

Formation and composition of organic aerosols from the uptake of glyoxal on natural mineral dust aerosols: a

laboratory study

Francesco Battaglia^{1,a}, Paola Formenti^{1,a}, Mathieu Cazaunau³, Edouard Pangui³, Antonin Bergé³, Aline Gratien¹, Diana L. Pereira^{1,b}, Thomas Bertin³, Joel F. de Brito⁴, Manolis N. Romanias⁴, Vincent Michoud¹, Clarissa Baldo^{1,3}, Servanne Chevaillier³, Gael Noyalet³, Philippe Decorse⁵, Bénédicte Picquet-Varrault³, and Jean-François Doussin³

¹ Université Paris Cité and Univ Paris Est Créteil, CNRS, LISA, F-75013 Paris, France

² Yusuf Hamied Department of Chemistry, University of Cambridge, Lensfield Road, Cambridge, CB2 1EW, UK

³ Univ Paris Est Créteil and Université Paris Cité, CNRS, LISA, F-94010 Créteil, France

⁴ IMT Nord Europe, Institut Mines-Télécom, Université de Lille, Centre for Energy and Environment, 59000, Lille, France

⁵ Université Paris Cité, CNRS, Itodys, F-75013 Paris, France

^a now at Dipartimento di Scienze Chimiche, Università degli Studi di Padova, Padova, Italy

^b now at Institute for Atmospheric and Earth System Research, University of Helsinki, Finland

For submission to Atmos. Chem. Phys.

Corresponding author: P. Formenti (paola.formenti@lisa.ipsl.fr)

Abstract

The uptake of glyoxal on realistic submicron mineral dust aerosol particles from a natural soil (Gobi Desert) is investigated during experiments in a large simulation chamber, under variable experimental conditions of relative humidity (RH), irradiation, and ozone concentrations. The uptake of glyoxal on the dust particles starts as soon as the glyoxal is injected into the chamber. At 80% RH, the measured uptake coefficient of glyoxal on mineral dust is $\gamma = (9 \pm 5) \times 10^{-3}$. The totality of the mass of reacting glyoxal is transformed into organic matter on the surface of the dust particles. The uptake of glyoxal is accompanied by the appearance of marker peaks in the organic mass spectra and a persistent growth in the volume concentration of the dust particles. While the mass of the organic matter on the dust rapidly reverts to values prior to uptake, the organic composition of the dust is modified irreversibly. Glycolic and other organic acids, but also oligomers, are detected on the dust. At 80% RH,

1. Introduction

Mineral dust originates naturally from the wind erosion of arid and semi-arid regions and the hydrolysis of particles suggests that dust reactions could play a role of substantial importance in the formation of organic aerosols at high RH, but also that the reaction could have potential implications for the dust optical and hygroscopic properties. Currently, the atmosphere is of the order of 4600 Tg yr⁻¹, accounting for approximately 40% of the total annual aerosol emissions (Knippertz and Stuut, 2014; Kok et al., 2021). Major natural source areas of mineral dust are North Africa (~50% of the global annual dust emissions), Asia (~40%), North America, and

the Southern Hemisphere (~10%; Kok et al., 2023). Anthropogenic emissions are associated with soil erosion for agriculture, pasture, and deforestation (Tegen and Fung, 1995; Webb and Pierre, 2018), but their contribution to the total annual dust mass loading is uncertain, ranging from 5 to 60% (Chen et al., 2023). Mineral dust significantly impacts the Earth's energy balance by absorbing and scattering radiation in the solar and terrestrial spectra (Di Biagio et al., 2019; Kok et al., 2023) and by influencing the lifetime and optical properties of mixed-phase and ice clouds (e.g., Atkinson et al., 2013; Harrison et al., 2001; Steinke et al., 2016). Current estimates of the effective radiative forcing (sum of direct and indirect) of natural mineral dust are in the range of $-0.07 \pm 0.18 \text{ W m}^{-2}$ (Kok et al., 2023), owing to large uncertainties in the atmospheric mass loading and properties of dust at emission and during transport (Castellanos et al., 2024; Li et al., 2021).

Gas-particle interactions along the dust lifecycle contribute to these uncertainties. Numerous laboratory and field studies show that mineral dust is capable to adsorb various reactive gaseous compounds, which may modify its chemical composition, and in turn to alter optical properties, hygroscopicity and ice nucleation activity but also may affect the oxidative capacity of the atmosphere (Bauer et al., 2007; Chirizzi, 2017; Crowley et al., 2010; Joshi et al., 2017; Liu et al., 2013; Ooki and Uematsu, 2005; Romanias et al., 2012; Seisel et al., 2004; Tang et al., 2017; Turpin and Huntzicker, 1995; Usher et al., 2003; Wagner et al., 2008). Dust aerosol may promote photocatalytic reactions of inorganic gases such as SO_2 and NO_2 , initiating nucleation events (Dupart et al., 2012; Nie et al., 2014).

The uptake of volatile organic compounds (VOCs) on mineral dust, such as limonene, toluene (Romanías et al., 2016), isoprene (Zeineddine et al., 2017), phenol (Hettiarachchi and Grassian, 2024), and dicarboxylic acids (Ponczek et al., 2019), is also documented. These reactions may alter the VOC budget in the atmosphere and lead to the formation of secondary organic aerosols (SOA) (Li et al., 2019; Tang et al., 2017; Usher et al., 2003; Xu et al., 2023; Zeineddine et al., 2023), one of the key players of atmospheric chemistry (Shrivastava et al., 2017).

Glyoxal (CHOCHO) is one of the most abundant VOCs in the troposphere (Lewis et al., 2020). It is produced through the oxidation of aromatic compounds like benzene, toluene, and p-xylene (Volkamer et al., 2001) as well as by the photochemical oxidation of isoprene (Chan et al., 2017). The global atmospheric concentrations of glyoxal have

86 been evaluated in the range of 10 – 100 pptv by Fu et al. (2008). However, case studies
87 show sometimes higher concentrations. During a field study in Shanghai in the summer
88 of 2018, Guo et al. (2021) reported an average glyoxal concentration of 164 ± 73 pptv,
89 due to daytime photochemistry. Local concentrations of up to 400 pptv have been
90 documented in regions influenced by aromatic pollution (Li et al., 2022). Satellite
91 measurements of glyoxal show that the highest concentrations in tropical and sub-
92 tropical regions are found during warm, dry periods influenced by biogenic emissions
93 and vegetation fires, but also anthropogenic pollution (Vrekoussis et al., 2009).
94 Elevated glyoxal concentrations have been observed in aged biomass burning plumes
95 and tropical ocean regions, revealing model under-predictions in high-emission areas
96 due to missing complex organic compound sources (Kluge et al., 2023). Field
97 measurements in the northeast Atlantic Ocean reveal that models generally
98 underestimate glyoxal concentrations due to missing contributions from acetaldehyde
99 and other chemical precursors, and a potential glyoxal source from the ocean surface
100 organic microlayer, particularly significant at night (Walker et al., 2022).

101 Glyoxal is a very soluble molecule which readily oligomerises in water, leading to the
102 formation of larger molecules (Kalberer et al., 2004; Shapiro et al., 2009). Several
103 previous studies have revealed that glyoxal can be taken up onto aerosol particles,
104 potentially serving as a significant source of organic aerosols (e.g., Liggio et al., 2005b;
105 Carlton et al., 2007; Ervens and Volkamer, 2010; Galloway et al., 2009; Knote et al.,
106 2014). The uptake of glyoxal on ammonium sulphate particles can lead to the formation
107 of carbon-nitrogen compounds (such as imidazole derivatives), oligomers, and organic
108 acids (Galloway et al., 2009), that has been observed to cause browning (De Haan et
109 al., 2020). The light-absorbing imidazole derivatives formed by glyoxal have been
110 found to act as a photosensitizer, initiating radical chemistry under realistic irradiation
111 conditions in the aerosol phase and initiating aerosol growth in the presence of
112 limonene (Rossignol et al., 2014).

113 The study by Shen et al. (2016) revealed that glyoxal can also uptake onto synthetic
114 minerals proxies of natural mineral dust, forming oligomers, organo-sulphates, formic
115 acid, and glycolic acid, henceforth suggesting a potential significant mechanism for
116 organic aerosol formation and modification of the optical and hygroscopic properties of
117 mineral dust. Recently, Zogka et al. (2024) highlighted the dependence of the soil

composition and size for the uptake of glyoxal on soils and soil surrogates (synthetic mineral).

Following up from those studies, in this paper we present novel laboratory experiments using a large-scale simulation chamber to investigate the formation of organic aerosol from the uptake of glyoxal on realistic airborne mineral dust particles, in atmospherically-relevant conditions. Dust aerosols are generated from a natural parent soil from the Gobi Desert, one of the most important sources of tropospheric dust and representative of an area where this interaction could take place (Wang et al., 2015).

This paper has two major objectives. First, it provides experimental observations of the uptake of glyoxal on mineral dust aerosol, leading to the formation of organic aerosol mass upon interaction and measuring glyoxal uptake coefficient of mineral dust. Secondly, it presents the chemical composition of the mixed organic-dust aerosols, in terms of their oxidation state, molecular composition and the evolution of SOA content from glyoxal.

2. Experiments and methods

This study uses the CESAM atmospheric simulation chamber (CESAM – Chambre de Simulation Atmosphérique Multiphasique, which translates to Experimental Multiphase Atmospheric Simulation Chamber in English), a 4.2 m³ cylindrical stainless-steel reactor initially described by Wang et al. (2011). CESAM was specifically designed to study multiphase processes involving aerosol particles, gas-phase compounds and water, both in the vapour and liquid phases (Brégonzio-Rozier et al., 2016; Denjean et al., 2014; Giorio et al., 2017). CESAM is equipped with three 6.5 kW high-pressure arc xenon lamps (model EX-170GM3-E, IREM SpA, Borgone, Italy) and 6 mm Pyrex plate filters to mimic the solar radiation. A 50 cm stainless-steel four-blade fan located at the bottom of the chamber ensures a mixing time of about 1 minute for the gas phase and the homogeneity of the internal composition.

2.1. Injection and cleaning protocols

Dust aerosols were generated and injected into the chamber according to the protocol detailed in Battaglia et al. (2025) using a natural soil sample from the Gobi Desert (107.48°N; 36.49°E). Prior to use, the soil was sieved at 1000 µm and dried at 100°C for less than one hour to remove adsorbed water and contamination from volatile gases. A quantity ranging from 30 and 50 g was placed in a 1 L Büchner flask and

shaken at 100 Hz using a sieve shaker (Retsch® AS200) to simulate the saltation and sandblasting mechanisms through which wind erosion generates airborne dust in the real atmosphere (Di Biagio et al., 2017). An Aerodynamic Aerosol Classifier (AAC, Cambustion®) was placed between the dust generator and the chamber to inject monomodal dust centred between 300 and 400 nm in geometric diameter.

Glyoxal was prepared by heating a mixture of equal amounts of its trimer hydrate (Fluka® Analytical) and P₂O₅ (Sigma – Aldrich ReagentPlus®, 99%) at 150°C (Horowitz et al., 2001). The trimer decomposition occurs inside a vial connected to a vacuum gas manifold. Glyoxal was collected as yellow crystals in a second vial immersed in an ethanol – liquid nitrogen cold trap at around -90°C and then vaporised in a 2.1 L glass bulb to a controlled pressure. This vial was connected to the simulation chamber to inject the glyoxal through a pure nitrogen flow.

Ozone was generated by a Corona discharge in pure O₂ using a commercial dielectric ozone generator (MBT 802N, Messtechnik GmbH, Stahnsdorf, Germany). Water vapour was generated by heating ultrapure water (Milli-Q IQ 7000, Merk™) inside a pressurised stainless-steel vessel, previously rinsed at least three times. The total organic carbon (TOC) content of the ultrapure water was monitored to evaluate the influence on the production of organic particles, which was found to be minor (see **Text S1** and **Figures S1 and S2** in the Supplementary Material). The relative humidity (RH) inside the chamber was measured by a HMP234 Vaisala® humidity and temperature transmitter. Before each experiment, the chamber was evacuated down to 10⁻⁴ mbar and then filled with a mixture of 80% N₂ (Messer, purity > 99.995%) and 20% O₂ (Linde 5.0, purity 99.999%) to an internal pressure exceeding by about 5 to 10 mbar the room atmospheric pressure, to prevent accidental contamination during the experiments.

2.2. Instrumentation

The CESAM chamber was equipped with a suite of standard instrumentation for the detection of the aerosol and the gas phase, whose details are reported in **Table S1**.

Gas-phase glyoxal was measured by a combination of in-situ long-path Fourier Transform Infra-Red (FTIR) spectrometry (Bruker Tensor 37) in the 2720-2930 cm⁻¹ absorption band corresponding to the C–H bonds, by a Cavity Attenuated Phase Shift (CAPS) NO₂ analyser (Model T500U, from Teledyne API) and a Proton Transfer Reaction-Time Of Flight-Mass Spectrometer (PTR-ToF-MS) (KORE Technology®,

second generation) operated in H_3O^+ ionization mode for VOC detection. The FTIR spectrometer also provided the concentrations of formic acid (HCOOH), measured in the C-O bond vibration band centred at 1105 cm^{-1} ; ozone (O_3), measured in the asymmetric stretching of the absorption band centred at about 1043 cm^{-1} ; and carbon monoxide (CO), detected at about 2143 cm^{-1} . The standard infrared absorption spectra of the compounds used for quantification, along with the specific absorption bands integrated for their quantification, are shown in **Figure S3**. CO and carbon dioxide (CO_2) were additionally measured by an APEE ProCeas[®] analyser. Nitrogen oxides (NO_x) were monitored by the APNA-370 analyser by Horiba[®].

The aerosol total number concentration above 2.5 nm was measured by a Condensation Particle Counter (TSI[®] model 3075). The aerosol number size distribution in the submicron fraction was measured by a combination of a Scanning Mobility Particle Sizer (SMPS) consisting of a Differential Mobility Analyser (TSI[®], model 3080) coupled with a Condensation Particle Counter (TSI[®] model 3072) and an Optical Particle Counter (sky-GRIMM[®] OPC model 1.109).

The aerosol chemical composition was measured by a combination of online and offline methods. A Time-of-flight Aerosol Chemical Speciation Monitor (ToF-ACSM, Aerodyne Research Inc.) equipped with a standard vaporiser provided quantitative unitary mass resolution spectra between 40 nm and $1\text{ }\mu\text{m}$ vacuum aerodynamic diameter (Fröhlich et al., 2013). The instrument was operated through a Nafion membrane dryer (model PD-50T-12). The organic mass concentration (m_{org}) was obtained considering a unitary collection efficiency ($\text{CE} = 1$) and a relative ionization efficiency (RIE) of 1.4 (Nault et al., 2023).

The glyoxal fragment CH_2O^+ at $m/z\ 30$ has an isobaric interference with the NO^+ fragment from nitrate. Following Galloway et al. (2009), the contribution of nitrate to the total signal at $m/z\ 30$ was calculated as 1.7 times the intensity of the nitrate signal at $m/z\ 46$, which corresponds to the 30/46 signal ratio measured during nitrate calibration. The contribution to $m/z\ 30$ of glyoxal was then calculated from the total signal by subtracting the contribution of the nitrate and the contribution of air. The elemental ratios of the organic fraction O/C and H/C are calculated from the measured f_{44} and f_{43} , respectively, following the parametrizations proposed by Aiken et al. (2008) and Ng et al. (2011), respectively.

Filter samples were collected on PTFE filters (Zefluor, 47 mm diameter, 2 μ m pore size, Pall Life Sciences) and quartz fiber membranes (Tissuquartz 2500 QATUP, 47 mm diameter, Pall Life Sciences) using a series of custom-made stainless-steel holder of 6-mm diameter operated at 10 L min⁻¹, and preceded by an denuder filled with active charcoal paper to remove ozone and VOCs. The sampling time ranged from 30 minutes to 3 hours. The filter holders and PTFE filters were pre-cleaned with dichloromethane (99.8 %, HPLC grade) in an ultrasonic bath, while the quartz filters were pyrolyzed at 550°C for approximately 8 hours. After sampling, filters were folded and placed in an aluminium paper envelope previously pyrolyzed (same protocol as the filters) and stored in a refrigerator at -18°C. Chamber blanks were collected by sampling for about 20 min from the chamber only filled with N₂ and O₂. Analytical blanks were also collected.

2.3. Filter analysis

The analysis of the filter samples was conducted by a combination of three techniques to provide a comprehensive view of the chemical composition of the organic fraction formed on the dust particles as the result of the processing by glyoxal. The full details of the analysers and analytical protocols are reported in as detailed in **Text S2** in the supplementary material. Those include

- 1/ the Supercritical fluid extraction coupled with gas chromatography mass spectrometry (SFE/GC-MS; Chiappini et al. (2006)) for target analysis of low-weight mass fragments derived from molecules linked to glyoxal reactivity (see **Table S2.1** in the Supplementary Material). such as the m/z 131 fragment (Glyoxylic acid TMS derivatized – CH₃), and the m/z 205 fragment (Glyoxal monohydrate – CH₃);
- 2/ Electrospray ionization (ESI) high-resolution mass spectrometry (Kourtchev et al., 2015) was used to obtain high-resolution mass spectra and formulae assignments for low-volatility compounds in the ranges m/z 50–500 and m/z 150–1000 (Zielinski et al., 2018). These were processed to provide parameters describing the carbon oxidation, through O/C and H/C bulk ratios, and the identification of molecular groups such as CHO, CHON, CHOS, CHNS, and CHONS. ESI-HR-MS was also used for a screening analysis of molecules resulting from the glyoxal transformation due to hydration, oxidation, and oligomerization. These included formulas for mono- and dihydration products

(C₂H₄O₃ and C₂H₆O₄, respectively), oxidation products (formic acid (CH₂O₂), glycolic acid (C₂H₄O₃), glyoxylic acid (C₂H₂O₃), and oxalic acid (C₂H₂O₄)), and oligomers formed by the hydrolysis of hydrated glyoxal formulas (linear oligomers with generic stoichiometric formula C_{2n+2m}H_{4n+6m-2(n+m-1)}O_{3n+4m-(n+m-1)}, and ring oligomers with generic formulae C_{2n+2m}H_{4n+6m-2(n+m)}O_{3n+4m-(n+m)}).

3/ X-ray photoelectron spectrometry (XPS) was used following Denjean et al. (2015) to quantify the elemental O/C ratio of the particle surface (O/C_{surf}) to a depth of less than 10 nm. The O/C_{surf} was calculated as explained in Text S2 in the Supplementary Material. The XPS measurement on a filter collected during one ageing experiment is shown as an example in **Figure S4** in the Supplementary Material.

2.4. Calculation of the aerosol size distribution

The procedure for combining the measurements of the SMPS and the sky-GRIMM[®] OPC is based on Baldo et al. (2023) and described in detail in Battaglia et al. (2025). The number size distributions, expressed in dN/dlogD (cm⁻³), are used to evaluate the total particle surface S (μm² cm⁻³) and volume V (μm³ cm⁻³) by assuming spherical particles as

$$S = \int \pi D^2 \frac{dN}{d\log D} d\log D \quad (2)$$

$$V = \int \frac{\pi}{6} D^3 \frac{dN}{d\log D} d\log D \quad (3)$$

2.5. Calculation of the glyoxal uptake coefficient and rate of particle formation

The uptake coefficient (γ) is defined as the probability of the gas to be taken up on the aerosol surface. It is a unit-less parameter expressed by the ratio between the number of molecules taken up on a surface and the total number of collisions of the gas on the surface as

$$\gamma = \frac{\text{number of total molecules taken up}}{\text{total number of collisions}} \quad (4)$$

The gas-phase uptake coefficient (γ) was estimated from the first-order heterogeneous loss rate of glyoxal (k_{het} , s⁻¹) as

$$\gamma = \frac{k_{het}}{\omega} \quad (5)$$

The rate of collisions (collision frequency, ω) is defined as

$$\omega = \frac{cA_s}{4} \quad (6)$$

where:

- $c = 146 \times \sqrt{\frac{T}{MW}}$ is the mean molecular speed (m s⁻¹), where T is the air temperature (here 298 K) and MW the molecular weight of the compound of interest (in the case of glyoxal MW = 58 g mol⁻¹).
- A_s is the total aerosol surface concentration (m² m⁻³).

The total aerosol surface concentration (A_s) is calculated from the aerosol size distribution recorded at the end of the dust injection.

The heterogeneous loss rate of glyoxal (k_{het}) due to its uptake on dust particles can be determined as the difference between the loss rate of glyoxal measured during the uptake experiments (k_{obs}) and the glyoxal loss rate on the chamber walls (k_{loss}) as

$$k_{het} = k_{obs} - k_{loss} \quad (7)$$

The glyoxal wall loss is represented by a partition equilibrium described by two first-order reactions: one for the adsorption of gas-phase molecules onto the chamber walls, and one for the reverse process. The rate constants for both processes have been obtained experimentally through control experiments with only glyoxal in the chamber and at different relative humidity conditions, as detailed in **Text S3** and Figures S5 to S9 in the supplementary material.

If the uptake reaction is of the first rate, k_{het} is henceforth calculated as

304

$$k_{het} = \frac{\ln\left(\frac{[Gly]_0}{[Gly]_{obs}}\right) - \ln\left(\frac{[Gly]_0}{[Gly]_{loss}}\right)}{t} \quad (8)$$

306

307 where $[Gly]_0$ is the initial concentration of glyoxal, $[Gly]_{obs}$ represents the observed
 308 evolution of glyoxal concentration in time, resulting from the sum of uptake and wall
 309 loss, and $[Gly]_{loss}$ represents the estimated glyoxal concentration resulting from the wall
 310 loss.

311 The rate of formation of the particulate organic matter (POM; k_{F-POM}) due to the uptake
 312 of glyoxal on the dust can be calculated as

313

$$k_{F-POM} = \frac{\ln\left(\frac{[POM]_t}{[POM]_0}\right)}{t} \quad (9)$$

315

316 where $[POM]_0$ represents the initial POM concentration in the particle phase, and
 317 $[POM]_t$ represents the concentration of the POM formed at a given time.

318 In the hypothesis that the POM formation is solely due to the uptake of glyoxal, γ can
 319 also be evaluated as

$$\gamma = \frac{k_{F-POM}}{\omega} \quad (10)$$

321

322 3. Results and discussion

323 3.1. Overview of experiments

324 The ageing experiments of monodispersed mineral dust and glyoxal described in this
 325 paper are summarised in **Table 1**. All the aerosol data are corrected for dilution, wall
 326 loss, and particle loss through the tubing systems as detailed in **Text S4** and Figures
 327 S10 and S11 in the Supplementary Material. Gas phase concentrations are corrected
 328 for dilution only.

329

Table 1. Listing and initial conditions of the experiments considered in this study, including experiments with glyoxal only (experiment type GL), ammonium sulphate and glyoxal (AS + GL), dust only (D) and dust with glyoxal (D + GL). The glyoxal and ozone gas phase concentrations correspond to the maximum value measured by FTIR after the respective injections. V_{seed} indicates the maximum volume concentrations of seed particles (either dust or ammonium sulphate) measured after the particle injection. The notation “dark/light” indicates experiments when filter samples were collected both in the dark and with irradiation.

Experiment type	Reagents	Date	Experiment number	RH, %	Light	[O ₃], ppb _v	Temp, K	[GL], ppb _v	V_{seed} , $\mu\text{m}^3 \text{cm}^{-3}$
Control	GL	29/04/2021	G ₁	< 5	dark	---	292	1130	---
		11/02/2022	G ₂	77	light	1440	291	627	---
	AS+GL	21/02/2023	AS ₁	38	dark	---	298	527	50.1
		23/02/2023a	AS ₂	35	dark	---	298	516	48.3
		23/02/2023b	AS ₃	32	light	---	298	445	64.8
		07/09/2023	AS ₄	81	light	---	301	779	304.1
		08/09/2023	AS ₅	83	light	---	300	430	161.2
	D	31/01/2022	D ₁	< 5	dark/light	---	292	---	31.5
		03/02/2022	D ₂	75%	dark/light	---	293	---	55.4
Uptake	D+GL	04/02/2022	D ₃	< 5	dark/light	---	293	690	35.6
		08/02/2023	D ₄	32	dark	---	294	940	21.5
		09/02/2023	D ₅	31	light	---	295	1050	52.7
		10/02/2023	D ₆	35	dark	---	294	809	37.4
		13/02/2023	D ₇	34	light	---	296	850	51.3
		30/04/2021	D ₈	76	light	---	289	759	28.3
		03/05/2021	D ₉	79	light	---	290	607	38.7
		04/05/2021	D ₁₀	81	light	---	290	371	31.5
		05/05/2021	D ₁₁	78	dark	---	291	805	30.1
		06/05/2021	D ₁₂	82	dark	---	292	432	21.1
		08/02/2022	D ₁₃	81	dark/light	1270	293	555	64.0
		09/02/2022	D ₁₄	78	dark/light	1450	293	756	79.8
		10/02/2022	D ₁₅	75	dark/light	---	295	600	68.4
		14/02/2023	D ₁₆	83	dark	---	296	661	35.8
		15/02/2023	D ₁₇	75	light	---	298	444	41.0

Table 1 also lists the few control experiments using ammonium sulphate as seed particles, described in detail in **Text S5** and Figures 12 to 14 in the Supplementary Material. No POM formation was observed during control experiments with dust or glyoxal only, both dry and humid conditions and with and without irradiation.

3.1.1. Timeline of particle concentration and composition

The ageing experiments lasted up to five hours. For the experiments carried out in wet conditions, the injection of water vapour preceded the injection of dust. The injection of glyoxal (nominal concentration of 1 ppmv) was conducted at least 30 minutes after the dust to ensure that the dust particles were homogeneously distributed in the reactor. Irradiation was started within one hour after the glyoxal uptake onto the particles. In a

few experiments, ozone was injected before glyoxal to verify the sensitivity of the reactions to the presence of an oxidant.

The typical timelines of the particle concentrations (number and volume) and the non-refractory composition measured in dry conditions and at 30% and 80% relative humidity are shown in **Figure 1**.

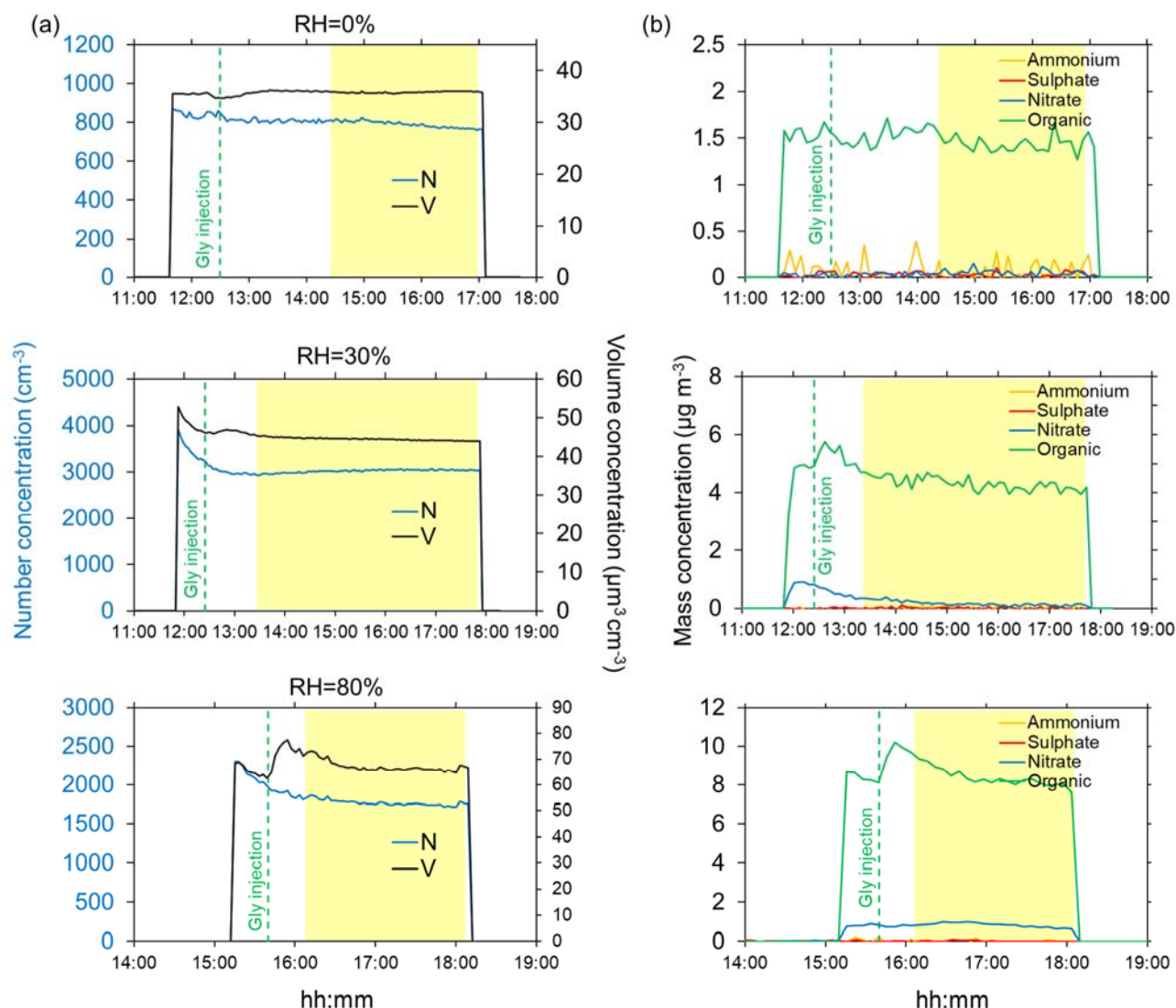


Figure 1. Timeline of ageing experiments of submicron dust with gas-phase glyoxal in dry conditions (top, experiment D₃), 30% (middle, experiment D₇), and 80% RH (bottom, experiment D₁₅). Left (a): aerosol total number (N) and volume (V) concentrations (blue and black lines, respectively) calculated from the measured dust size distributions. Right (b): mass concentrations of ammonium, sulphate, nitrate and organic (yellow, red, blue and green lines, respectively) measured by the ACSM. The yellow-highlighted portion of the graph indicates the interval where irradiation takes place, while the green vertical dashed lines indicate the injection of glyoxal in the chamber. The dust injection corresponds to the time of the initial increase of the number and volume concentrations. Aerosol time series are corrected for dilution, wall loss and particle loss through the tubings.

Figure 1 shows that in dry conditions, there is no significant variation of either the aerosol number or the volume concentrations, nor the chemical composition (including organics) following the glyoxal injection.

At 30% RH, a small increase in the total volume concentration (approximately $5 \mu\text{m}^3 \text{cm}^{-3}$) is observed for about 30 minutes after the injection of glyoxal. This corresponds to an increase of the POM of about $1 \mu\text{g m}^{-3}$, approximately 20% more with respect to the value measured before the uptake. On the other hand, the particle number concentration shows an apparent decrease at the beginning of the experiments, possibly because the particle loss correction model of Lai and Nazaroff (2000) does not fully apply to dust particles and humid conditions (see discussion in Battaglia et al. (2025)). After that, and through the duration of the experiment, however, it remains constant, indicating that the increase in the particle volume occurs on the dust particles and not because of new particle formation.

At 80% RH, the increase in both the total volume and the POM concentrations is more pronounced, approximately $10\text{-}15 \mu\text{m}^3 \text{cm}^{-3}$ and $2 \mu\text{g m}^{-3}$, respectively. As for 30% RH, both total particle volume and the POM concentrations return to values observed prior to the injection of glyoxal, within approximately 30 minutes from their maximum values, likely due to evaporation. A similar behaviour is observed in the presence of ozone (**Figure S15** in the Supplementary Material). As for 30% RH, the particle number concentration slightly decreases in time at the beginning of the experiment, but then remains constant, again excluding the formation of new particles but rather confirming the formation of organic matter on pre-existing particles. This is also supported by the fact that the rate of increase of POM and particle volume is the same (slope $3.2 \times 10^{-4} \text{ s}^{-1}$ and $3.2 \times 10^{-4} \text{ s}^{-1}$, respectively, for POM and total volume), as shown by **Figure S16** in the Supplementary Material.

3.1.2. Timeline of gas-phase concentration

Figure 1 also shows that, while sulphate and ammonium are never detected, a background concentration of nitrate up to $1 \mu\text{g m}^{-3}$ is measured by the ACSM as soon as the dust particles are injected in the presence of water. We attribute it to the heterogeneous interaction between NO_2 and the dust particles (Goodman et al., 1999), as indeed, a background concentration of a few ppb of NO_2 is present in the chamber as a result of the procedure used to reduce the TOC content in the injected water (see **Figure S17** in the Supplementary Material). However, since the contribution of nitrate

represents at maximum 1% of the injected dust mass and it decreases or remains constant throughout the experiment, its contribution to the particle growth and overall ageing of the mineral dust should be negligible.

Figure 2 shows the time series of the gas-phase compounds detected during the same experiment (D₁₅) at 80% RH.

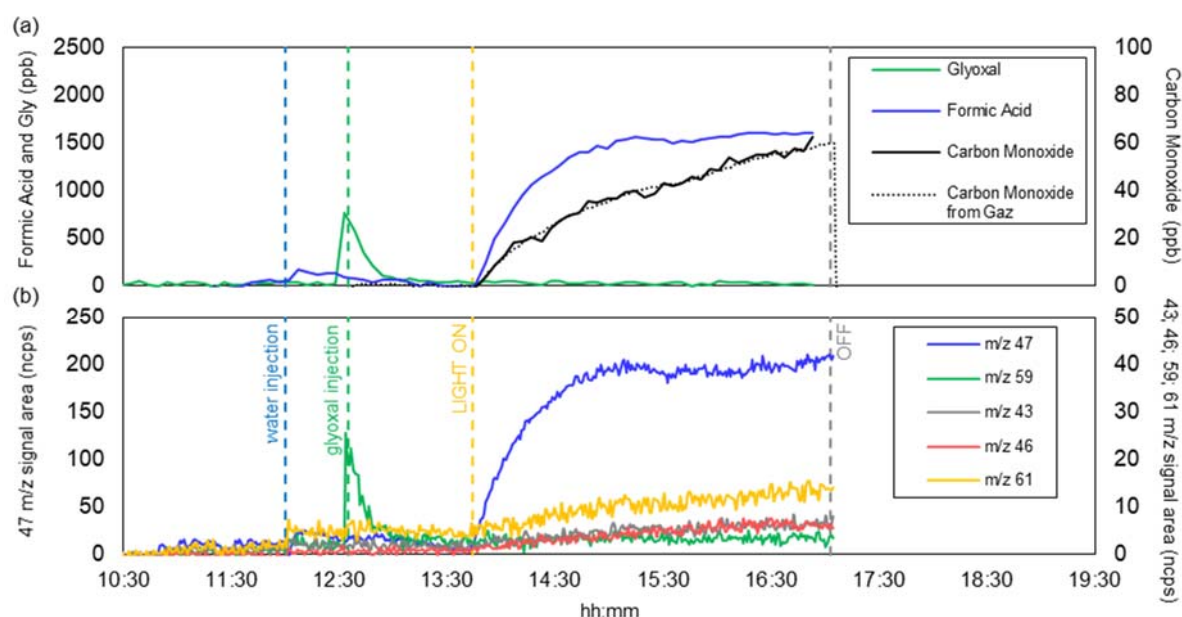


Figure 2. Time series of the gas-phase composition observed during experiment D₁₅: (a) concentrations of carbon monoxide, glyoxal and formic acid measured by FTIR (for CO, the measurements of the online analyser are also shown); (b) various VOC ions (m/z 47, 59, 43, 46 and 61) measured by the PTR-MS. Ion signals measured by PTR-MS are normalized by signals of reagent ions (i.e. H_3O^+ and $H_3O^+(H_2O)$) and therefore expressed in normalized counts (ncps). The blue vertical dashed lines indicate the injection of water in the chamber; the green vertical dashed lines indicate the injection of glyoxal in the chamber, the yellow dashed lines indicate the beginning of irradiation, and the grey dashed lines indicate the end of irradiation.

The measured glyoxal concentration after the injection (**Figure 2a**) is lower than the nominal concentration of 1 ppm and goes to zero within minutes due to the rapid interactions with the walls of the chamber, water vapour, and the dust particles. Upon irradiation, formic acid and carbon monoxide are formed, as expected by the photolysis of glyoxal (De Haan et al., 2020). Fragments m/z = 46 and 47 are observed during water injection and photolysis, which could originate from the deprotonated and protonated form of formic acid, respectively. This suggests that a minor fraction of the formic acid could result from the desorption of compounds (including glyoxal) from the chamber walls. Fragments m/z = 43 and m/z = 61, and occasionally m/z = 45 (not seen

during experiment D₁₅ and therefore not shown in **Figure 2b**), are observed at a normalised intensity two orders of magnitude lower than that of formic acid, but not attributed. The quantification with both PTR-MS and FTIR in our experimental RH conditions is complex due to water presence, which reduces the sensitivity of PTR-MS and can interfere with the absorption of various organic compounds, making their quantification less accurate.

3.2. Evaluation of glyoxal uptake coefficient and rate of formation of organic aerosols

Figure 3 shows an example of the temporal evolution of the natural logarithm of the glyoxal concentration measured by the FTIR, compared to that measured during a typical blank experiment without dust particles (top panel) and the variation of the aerosol organic fraction measured by the ToF-ACSM during the same time period (lower panel).

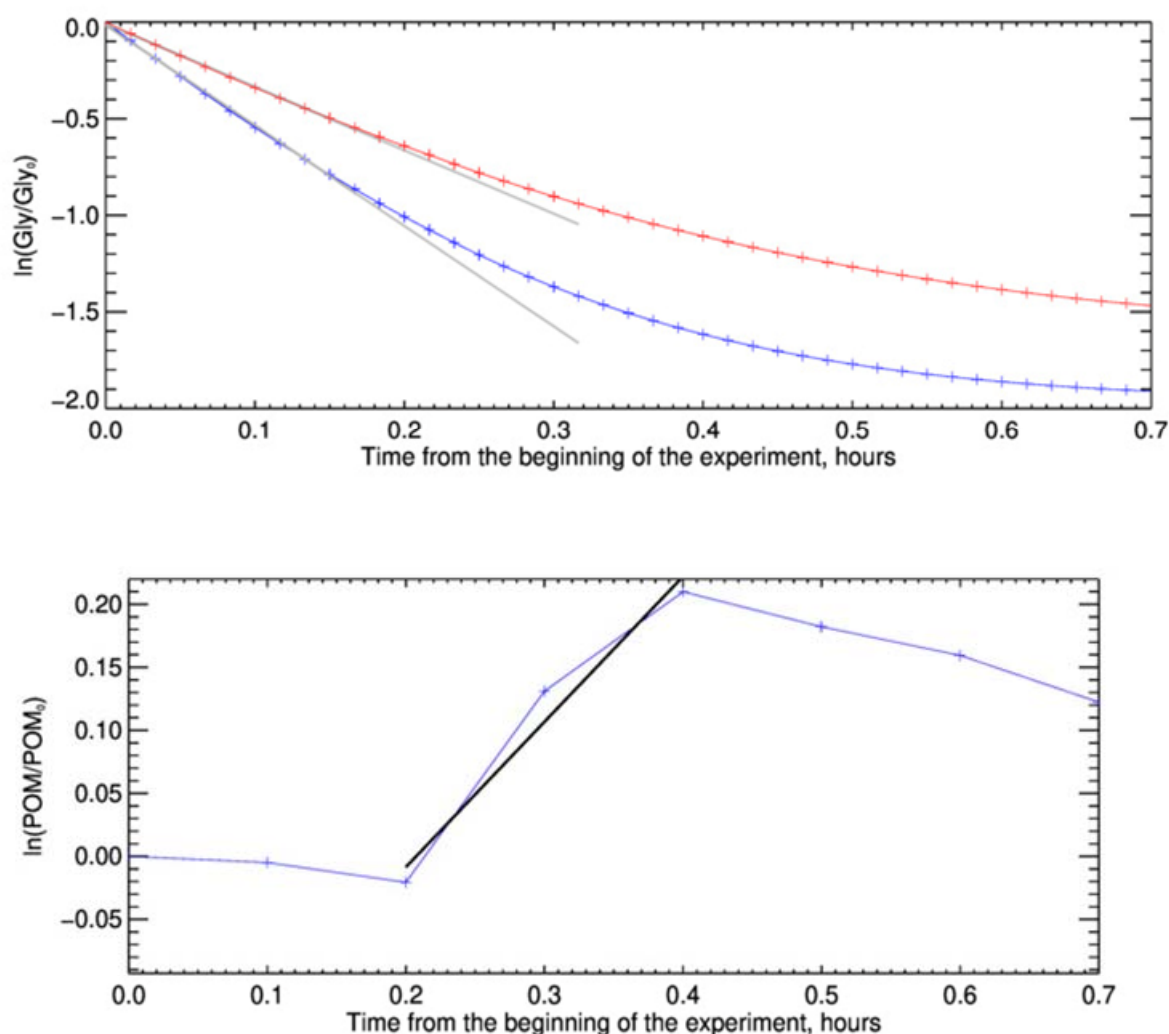


Figure 3. Measurement of glyoxal uptake coefficient on dust for the experiment D₁₅, conducted at 80% RH. The figure compares the two methods for measuring the uptake coefficient. In the top image, results are shown for the method based on monitoring the decay of gas-phase glyoxal. The red and blue curves represent the logarithm of the ratio between the calculated decay of gas-phase glyoxal in the absence and presence of dust aerosols, respectively. The black lines represent the linear fit whose slope provides the heterogeneous kinetic constants of the two processes. The image at the bottom displays the result of the uptake coefficient measurement for the same experiment, obtained from the organic formation on the dust aerosol monitored by the ToF-ACSM. The blue time series shows the logarithm of the ratio between the measured organic concentration divided by the initial organic on dust aerosol, while the black line is the linear fit representing the kinetics of organic formation.

Within the first 10 minutes after the injection of glyoxal, the decrease of the natural logarithm concentrations ratio with time in the presence of dust is linear (that is, the rate is constant). After that, the loss slightly deviates from linearity. The difference from linearity is more evident for the blank experiment, when it occurs earlier than when the dust is present. These observations indicate that, within the first 10 minutes, the uptake of glyoxal on the dust particles can be considered to follow a first-order kinetics and its rate represents an initial uptake coefficient. In the following 20 minutes approximately, the uptake slows down, possibly because all the sites available on the particle surface become occupied, but also because that desorption from the particle surface could reinject glyoxal into the reactive mixture. On the particle phase, the natural logarithm of the organic concentration, normalised by its initial value, increases rapidly and linearly, almost on the same time scale as that of the loss of glyoxal, but then decreases to return to its initial value within approximately one hour. These observations confirm that the uptake of glyoxal results in the formation of OA on the dust particles, but that this process is reversible.

The uptake coefficients calculated as the linear fit of the glyoxal and particle organic concentration are presented in **Table 2**.

Table 2. Uptake coefficients for glyoxal on mineral dust and ammonium sulphate calculated from the loss of gas-phase glyoxal ($\gamma_{\text{Gly-Dust-gas}}$) and the rate of OA formation ($\gamma_{\text{Gly-Dust-gas}}$) for the experiments conducted at 80% RH. The initial glyoxal concentration is reported. The aerosol surface concentration (A_s) corresponds to the value preceding the glyoxal injection. Ozone concentration is the maximum concentration measured by FTIR spectroscopy after the injection. For ammonium sulphate, only the γ values calculated from the loss of gas phase glyoxal are presented, as the ACSM collection efficiency (CE) for ammonium sulphate varies significantly during OA formation (Matthew et al., 2008).

Date	Experiment ID	RH%	[GL] ₀ , ppb _v	Ozone (ppb)	A_s (m ² m ⁻³)	ω (s ⁻¹)	$\gamma_{\text{Gly-Dust-gas}}$	$\gamma_{\text{Gly-Dust-OA}}$
30/04/2021	D ₈	76	759	---	4.8×10^{-4}	3.9×10^{-2}	6.0×10^{-3}	1.0×10^{-3}
03/05/2021	D ₉	79	607	---	6.1×10^{-4}	5.0×10^{-2}	1.5×10^{-2}	1.5×10^{-2}
04/05/2021	D ₁₀	81	371	---	5.1×10^{-4}	4.2×10^{-2}	1.7×10^{-2}	9.0×10^{-3}
05/05/2021	D ₁₁	78	805	---	4.6×10^{-4}	3.8×10^{-2}	8.0×10^{-3}	5.0×10^{-3}

06/05/2021	D ₁₂	82	432	---	3.5×10^{-4}	2.9×10^{-2}	1.2×10^{-2}	2.3×10^{-2}
08/02/2022	D ₁₃	81	555	1270	7.1×10^{-4}	5.8×10^{-2}	4.0×10^{-3}	4.0×10^{-3}
09/02/2022	D ₁₄	78	756	1450	8.5×10^{-4}	7.0×10^{-2}	4.0×10^{-3}	5.0×10^{-3}
10/02/2022	D ₁₅	75	600	---	8.4×10^{-4}	6.9×10^{-2}	1.0×10^{-2}	5.0×10^{-3}
14/02/2023	D ₁₆	83	661	---	6.0×10^{-4}	4.9×10^{-2}	4.0×10^{-3}	1.5×10^{-2}
07/09/2023	AS ₄	81	779	---	6.3×10^{-3}	5.2×10^{-1}	9.8×10^{-4}	---
08/09/2023	AS ₅	83	430	---	2.0×10^{-3}	1.7×10^{-1}	1.2×10^{-3}	---
Average dust							$9 (\pm 5) \times 10^{-3}$	$9 (\pm 7) \times 10^{-3}$
Average AS							$1.1 (\pm 0.2) \times 10^{-4}$	

The average uptake coefficients for glyoxal on the Gobi mineral dust calculated at 80% RH from the gas-phase uptake and the particle formation are $\gamma_{\text{Gly-Dust-gas}} = 9 \times 10^{-3}$ (standard deviation ± 5) and $\gamma_{\text{Gly-Dust-OA}} = 9 \times 10^{-3}$ (standard deviation ± 7), respectively. The two average values agree. This suggests that every glyoxal molecule in the gas phase is taken up by the airborne dust particles. This also suggests that the uptake occurs on airborne particles only, as expected, as the dust particles are selected in the submicron range and that minimal deposition of dust particles is observed in the first 30 minutes after injection. The primary mechanism of particle loss during this period is dilution, which does not interfere with uptake. The standard deviations of the mean values are large, being attributed to the fact that the state of the chamber walls and the dust size distribution vary from one experiment to the other, and that the aerosol/chamber walls surface ratio is very low ($0.08\text{--}1.5 \times 10^{-3}$).

The presence of ozone appears to be uninfluential. Hanish and Crowley (2003a) investigated the combined uptake of O_3 and HNO_3 onto dust and showed that the uptake of HNO_3 on dust was not influenced by the presence of O_3 (and conversely, the uptake of O_3 was not influenced by the presence of HNO_3). These authors attributed these observations to the fact that in their experiments, O_3 concentrations were in excess by more than three orders of magnitude with respect to those of HNO_3 , compensating for the fact that the uptake coefficients for O_3 is approximately four orders of magnitude lower than for HNO_3 (Hanish and Croley 2003b; Chang et al., 2005). In these conditions, which are not generally met in the atmosphere, the presence of O_3 could result in the modification of surface chemical characteristics or competition for adsorption sites of the two species. These considerations are applicable to our experiments, as the uptake coefficients of O_3 and glyoxal are of comparable magnitudes, and we use comparable concentrations.

3.3. Evidence of irreversible particle growth

Figure 1 shows that, even in the more favourable conditions (RH=80%), the ratio between the observed increase of the POM ($2 \mu\text{g m}^{-3}$) and that of the particle volume concentration ($20 \mu\text{m}^3 \text{cm}^{-3}$) corresponds to an estimated mass density of the order of 0.1 g cm^{-3} , which is about 10 times lower than the value of 1 g cm^{-3} expected for glyoxal. This is partially attributed to the fact that only part of the organic matter formed on dust is detected by the ACSM. On the other hand, **Figure S16** shows that, after reaching its maximum value, the volume concentration decreases at a lower rate than the POM (slope $3.9 \times 10^{-5} \text{ s}^{-1}$ and $6.1 \times 10^{-5} \text{ s}^{-1}$, respectively). This suggests that an additional process could contribute to the particle volume concentration, partially compensating for the loss of organic matter on the dust particles.

This is confirmed by **Figure 4**, which shows the variation in time of the normalised particle volume distributions, at four steps of the experiments performed at 30% RH and 80% RH. Those include prior and glyoxal injection, POM maximum peak value, and the end of the experiment.

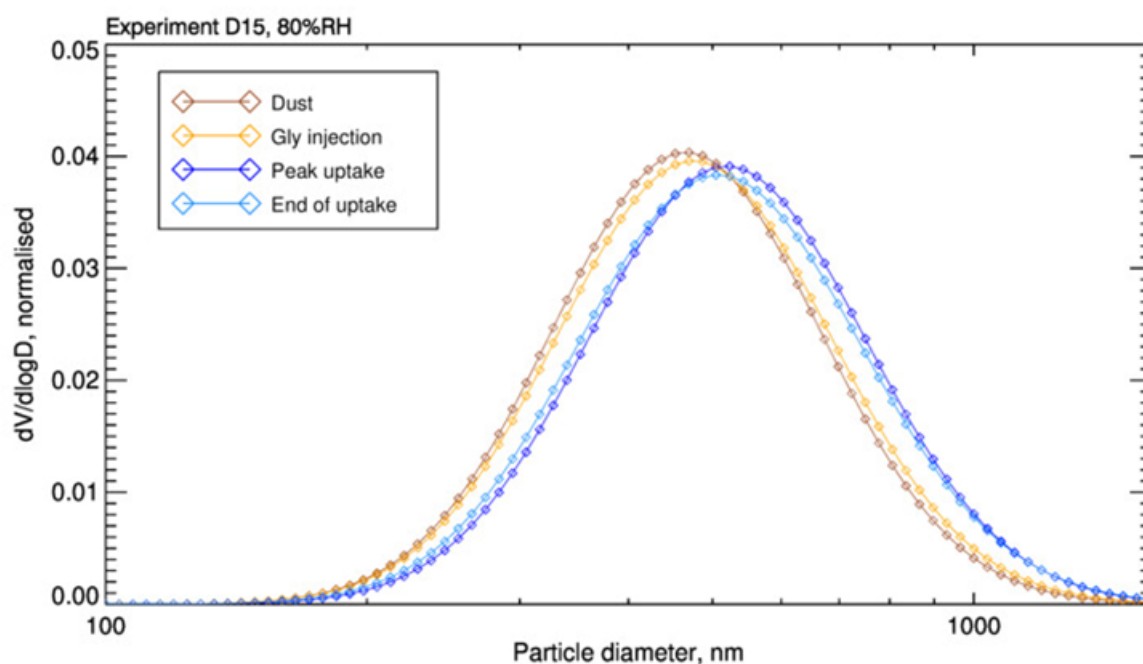
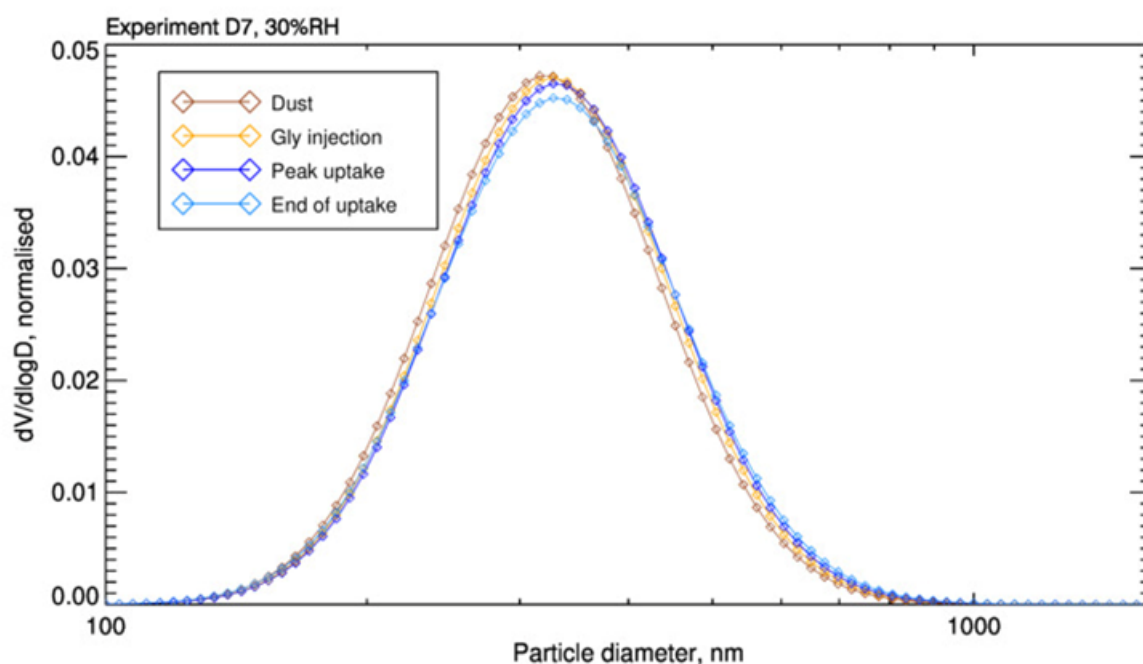


Figure 4. Evolution of volume-size distributions for two glyoxal uptake experiments in different relative humidity conditions. The images illustrate the progression of volume-size distributions recorded at four key moments during the experiments. The first distribution (orange) is recorded after the dust is injected into the simulation chamber. The second distribution (yellow) is recorded at the moment of glyoxal injection. The third distribution (blue) corresponds to the peak uptake of glyoxal on the aerosol, and the fourth (light blue) is recorded at the end of the glyoxal uptake process. The left image depicts the evolution for the experiment D7 conducted at 30% RH, while the image on the right shows the distributions for the experiment D15 conducted at 80% RH. The results highlight that the distributions grow more significantly at 80% RH, indicating a higher glyoxal uptake and organic formation at elevated humidity levels.

All distributions have a single mode. However, after the injection of glyoxal, the geometric mean volume diameter, measured at the maximum POM concentration, increases by up to 10% (from 310 to 340 nm) at 30% RH, and up to 20% (from 450 to 540 nm) at 80% RH. Interestingly, even at the end of the experiment, when the POM concentration returns to its initial value, the increase in geometric mean diameter of the aerosol is irreversible. We hypothesize that the uptake of glyoxal enhances the dust hygroscopicity. Therefore, the difference in total volume between the beginning and end of the experiment is due to formed organic aerosol mass, resulting from water uptake.

3.4. Chemical composition of the particulate organic matter

This section discusses the chemical composition of the particulate organic matter formed on the mineral dust following the interaction with glyoxal. The list and conditions of the filter samples analysed by SFE/GC-MS and ESI-Orbitrap are reported in **Table S2** in the Supplementary Material. Details of the organic composition of the native dust are provided in **Text S6 and Figures S18 to S20**.

3.4.1. Timeline of chemical evolution

Figure 5 shows the time evolution of the intensity of the organic fragments detected by the ToF-ACSM at 80% RH (experiment D₁₅) at four moments of the experiment: 1) before the injection of glyoxal; 2) during the uptake and the formation of the organic matter; 3) after the organic matter has reached its maximum concentration; and 4) at the end of the experiment, when the organic matter returned to its initial concentration.

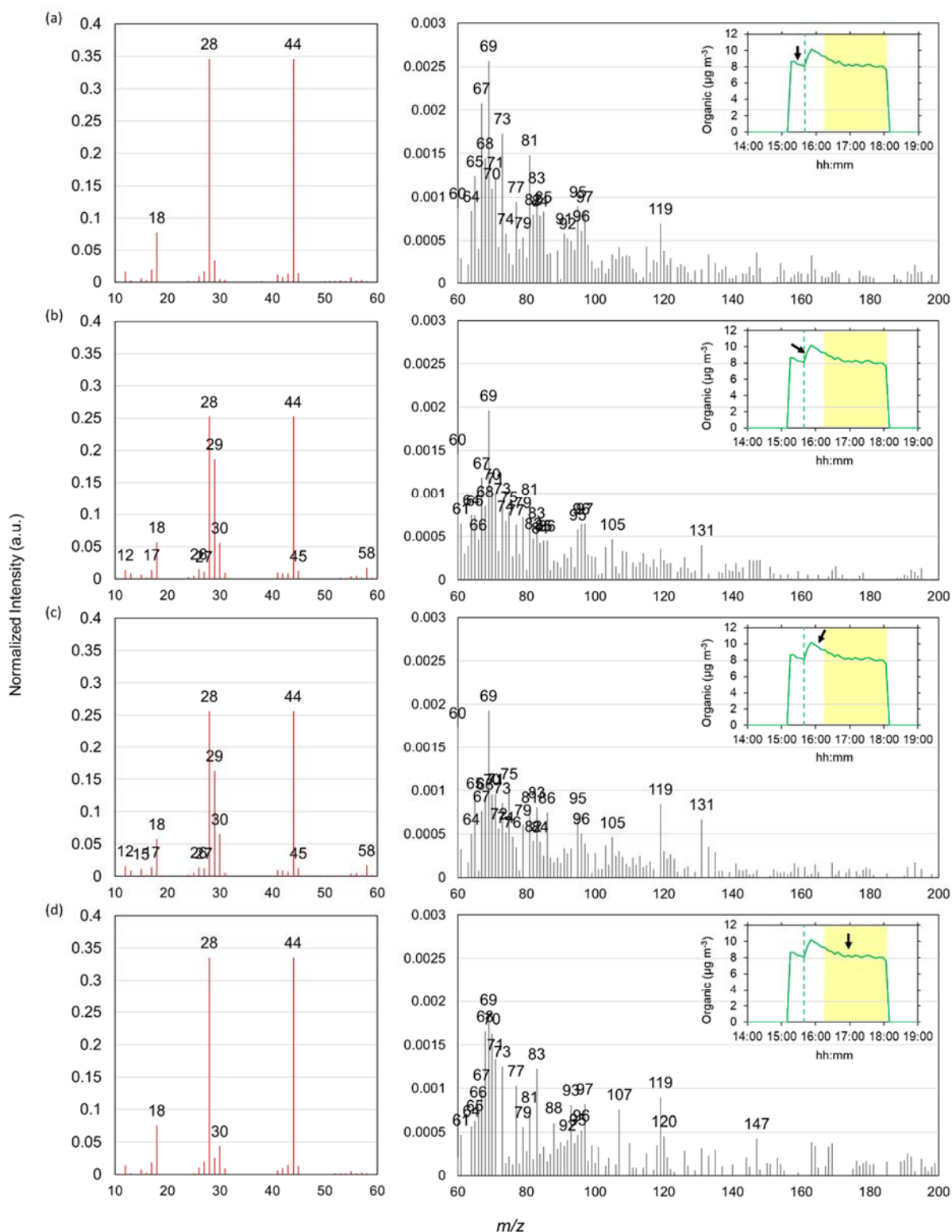


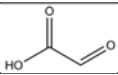
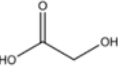
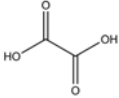
Figure 2. ACSM organic mass spectra (intensities normalized to the total organic concentration) recorded during the experiment D₁₅: (a) before glyoxal uptake (dust organic fraction composition), (b) during glyoxal uptake, (c) after reaching the maximum uptake on the particles and (d) 1h later under irradiation. Panels on the left show the mass spectra ranging from m/z 10 to 60, while the panels on the right represent fragments from m/z 60 to 200 (their intensity is approximately one hundred times lower). The inserts display the time series of organic concentrations measured by the ToF-ACSM. A black arrow indicates the time corresponding to the mass spectrum shown. The yellow-highlighted shaded area indicates the interval where irradiation takes place, while the green vertical dashed lines indicate the moment of glyoxal injection in the chamber.

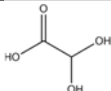
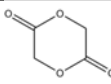
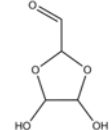
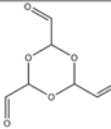
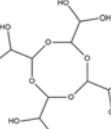
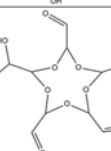
Figure 5 reveals that the organic matter formed as a result of the interaction between mineral dust and glyoxal is composed of oxidized organic fragments, organic acids, and oligomers. Oxidized organic fragments such as CO^+ (m/z 28) and CO_2^+ (m/z 44) are observed through all phases of the experiments. Fragments such as CHO^+ (m/z 29), CH_2O^+ (m/z 30), and $\text{C}_2\text{H}_2\text{O}_2^+$ (m/z 58) appear during the uptake of glyoxal, but diminish over time, due to oligomerization or further oxidation processes. The most intense fragment above m/z 60 is m/z 69, which appears unrelated to glyoxal reactivity but could be attributed to nitrogen-containing organic species such as $\text{C}_3\text{H}_3\text{NO}^+$, originating from glyoxal–ammonia reactions (Galloway et al., 2009) or plant and soil residues (Sun et al., 2010; Nieder et al., 2018). Fragments at m/z 105 and 131, observed consistently during the uptake and the photolysis, could be attributed to condensed glyoxal hydrates (Liggio et al., 2005; Carlton et al., 2007). Fragments at m/z 119 and 120, associated with oxidized products from isoprene-derived aerosols (Safi Shalamzari et al., 2013), increased after glyoxal uptake and under irradiation, suggesting the formation of oxidized oligomers. Upon irradiation, the appearance of m/z 147 and 165 – products of aqueous glyoxal oxidation and oligomer condensation (Lim et al., 2010) – suggests photo-chemically enhanced transformation, though their presence in native dust also points to reversible adsorption processes.

3.4.2. Molecular identification

The list and conditions of the samples analysed by SFE/GC-MS and ESI-Orbitrap are reported in **Text S7** and Figures S21 and S22 in the Supplementary Material, which also provides with examples of analysis. The summary of the organic molecules detected by those analysis is presented in **Table 3**.

Table 3. Summary of observed compounds identified by SFE/GC-MS analysis and glyoxal-related formulas observed with ESI-Orbitrap, along with the suggested structures under the different experimental conditions tested.

Molecular formula	Name	Tentative Structure	Technique	Experimental conditions
$\text{C}_2\text{H}_2\text{O}_3$	Glyoxylic acid		ESI-Orbitrap	Dust+Gly, 80%, Dark, O_3
$\text{C}_2\text{H}_4\text{O}_3$	Glycolic acid		ESI-Orbitrap SFE/GC-MS	Dust+Gly, 30%, Dark Dust+Gly, 30%, Light Dust+Gly, 80%, Light Dust+Gly, 80%, Light, O_3
$\text{C}_2\text{H}_2\text{O}_4$	Oxalic acid		ESI-Orbitrap	Dust+Gly, 80%, Light

$C_2H_4O_4$	Glyoxylic acid monohydrate		ESI-Orbitrap SFE/GC-MS	Dust+Gly, 80%, Light
$C_4H_4O_4$	Glycolic acid dimer		ESI-Orbitrap	Dust+Gly, 80%, Light
$C_4H_6O_5$	Glyoxal oligomer		ESI-Orbitrap	Dust+Gly, 80%, Light
$C_6H_6O_6$	Glyoxal oligomer		ESI-Orbitrap	Dust+Gly, 80%, Light
$C_8H_{16}O_{12}$	Glyoxal oligomer		ESI-Orbitrap	Dust+Gly, 80%, Light
$C_{10}H_{12}O_{11}$	Glyoxal oligomer		ESI-Orbitrap	Dust+Gly, 80%, Dark

585

586 Oxidized organic compounds such as glycolic acid ($C_2H_4O_3$), oxalic acid ($C_2H_2O_4$),
587 and a possible dimer of glycolic acid ($C_4H_4O_4$) were mainly observed under irradiated
588 conditions, while their hydrated forms also appeared in dark conditions. Glyoxylic acid
589 was detected in dark conditions in the presence of ozone. Glycolic and glyoxylic acids
590 consistently form under humid conditions, indicating that their pathways may be less
591 sensitive to water competition or that their precursors interact more strongly with dust
592 surfaces. Light but also ozone tends to favor the formation of glycolic acid from glyoxal
593 at high RH, suggesting two possible oxidative pathways. Glycolic acid is also detected
594 at 30% RH (not showed), with and without irradiation, in agreement with the
595 experiments on dust by Shen et al. (2016), but differently than reported by Galloway et
596 al. (2009) on ammonium sulphate. Monohydrated glyoxylic acid is found in one sample
597 at 80% RH under irradiated conditions, likely due to the known pattern of oxidation of
598 glyoxal and glycolic acid with OH radicals (Buxton et al., 1997). Unlike previous studies
599 (Galloway et al., 2009; Rubasinghege et al., 2013; Shen et al., 2016), formic acid was
600 not detected on the particle phase despite high concentrations observed in the gas
601 phase (**Figure 2**). It can be hypothesized that formic acid was not detected in the
602 particle phase due to the low amount of organic material on the filter samples and the
603 unsuitability of the method used (due to interferences at the retention time where formic
604 acid is expected).

Oligomerization products (compounds from C₄ to C₁₀) of the glyoxal mono- and dihydrate forms are observed only at 80% RH. These are: C₄H₆O₅ (1 monohydrated glyoxal + 1 dehydrated glyoxal forming a 5-atom ring), C₈H₁₆O₁₂ (4 dehydrated glyoxal molecules forming an 8-membered ring), and C₁₀H₁₂O₁₁ (4 monohydrated glyoxal molecules + 1 dehydrated glyoxal molecule forming a ring structure). The oligomer C₆H₆O₆ (3 molecules of monohydrated glyoxal forming a 6-membered ring) is detected only under dark conditions. C₈H₁₆O₁₂, can correspond to an oligomer previously observed by Shen et al. (2016) on mineral dust.

The persistence of low-volatility, heavy compounds, such as oligomers at the surface of mineral dust has implications for its oxidation state, which is modified in an irreversible way its surface composition, as already shown by previous studies on ammonium sulphate seeds (Kroll et al., 2005; Galloway et al., 2009; De Haan et al., 2020; Hu et al., 2022). This is illustrated by the van Krevelen diagrams obtained from the ESI-Orbitrap analysis in **Figure 6**.

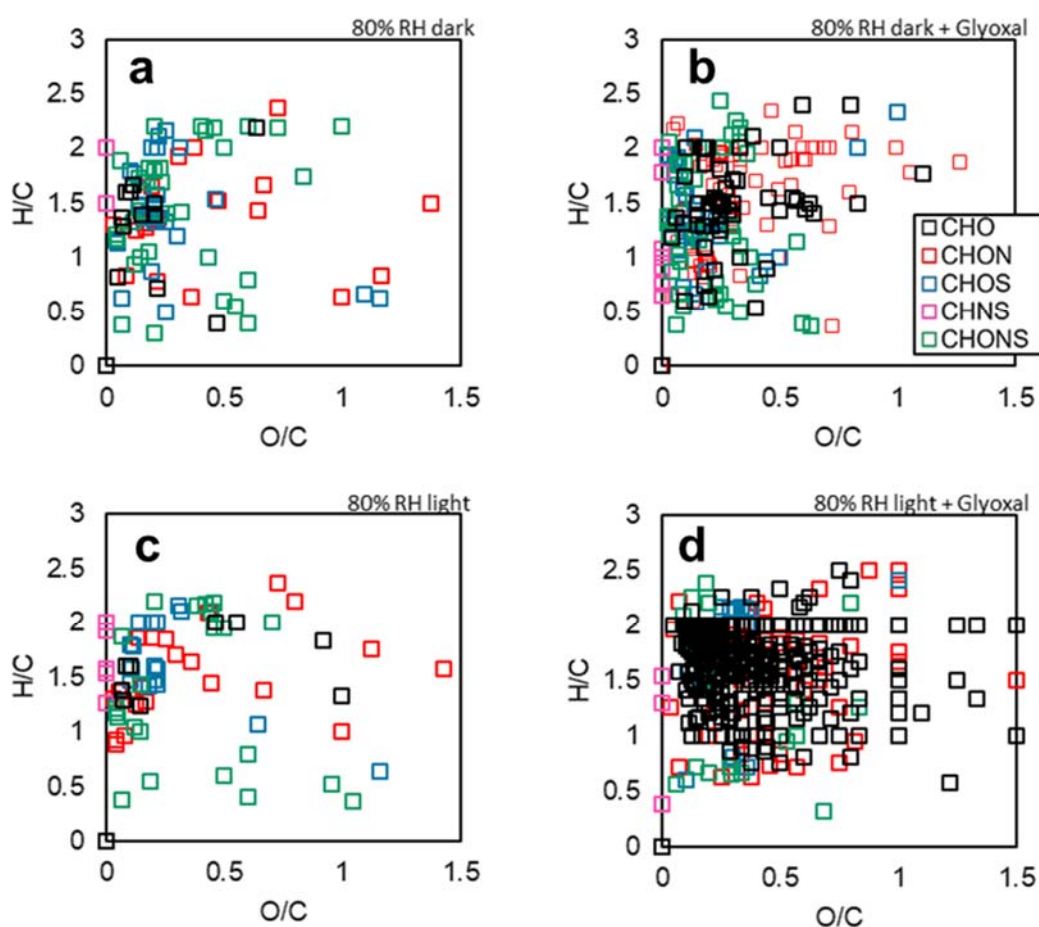


Figure 6. Van Krevelen diagrams recorded at 80% RH for: in the top line experiments in the dark for mineral dust only (control experiment D₂, left) and one ageing experiment of dust with glyoxal

(experiment D10); bottom line: same with irradiation. Samples are equivalent in terms of load of particulate organic matter. These are 0.9 μg (sample a), 0.8 μg (sample b), 1.7 μg (sample c) and 0.6 μg (sample d). Despite an equivalent loading of particulate organic mass, the number of signals detected is significantly higher when the dust is exposed to glyoxal (86 and 102 peaks detected for dust only against 398 and 310 with glyoxal, and with and without light, respectively).

The processing by the glyoxal clearly has an effect on the oxidation state of the dust, particularly when lights are on, resulting in the appearance of signals with O/C ratio higher than 1, attributed to photo-oxidation. The predominant family in this case is that of CHO molecules, while the appearance of molecules for families CHON and CHONS is also observed.

4. Discussion

4.1. Comparison of uptake coefficients

The uptake of glyoxal on the dust particles occurs in humid conditions exceeding 30% RH. These observations agree with the results of Liggio et al. (2005a; 2005b) on the uptake of glyoxal on ammonium sulphate aerosols, observing the formation of organic matter only when RH exceeded 50%. Trainic et al. (2011) also observed that the uptake of glyoxal on glycine and ammonium sulphate particles occurred only when the relative humidity was above 35%. On the contrary, both Shen et al. (2016) and Zogka et al. (2024) demonstrated that the uptake can occur in dry conditions too, which was not observed in this work.

At 80% RH, the experimental average of the measured uptake coefficient of glyoxal on mineral dust is $\gamma = (9 \pm 5) \times 10^{-3}$. Our values are approximately one order of magnitude higher than those obtained by Shen et al. (2016), who investigated the uptake of glyoxal on mineral proxies, i.e. SiO_2 , CaCO_3 and $\alpha\text{-Al}_2\text{O}_3$ under various levels of RH. These authors determined the uptake coefficients after a long exposition of the surface to glyoxal (steady state uptakes) and found that the uptake coefficients decrease with increasing gas phase concentration of glyoxal. At 1 ppb concentration and 60% RH, the uptake coefficient determined on suspended particles of calcite (CaCO_3) is $1.4 (\pm 0.1) \times 10^{-4}$ and $5.5 \pm (0.1) \times 10^{-5}$ on alumina ($\alpha\text{-Al}_2\text{O}_3$).

Zogka et al. (2024) used a Knudsen cell to evaluate the initial and steady-state glyoxal uptake coefficient bulk soil samples of various origins. At low RH, these authors found that for Gobi soil sieved to less than 63 μm in diameter, the initial uptake coefficient using the geometric surface area was 0.18 (corresponding to an upper limit of the

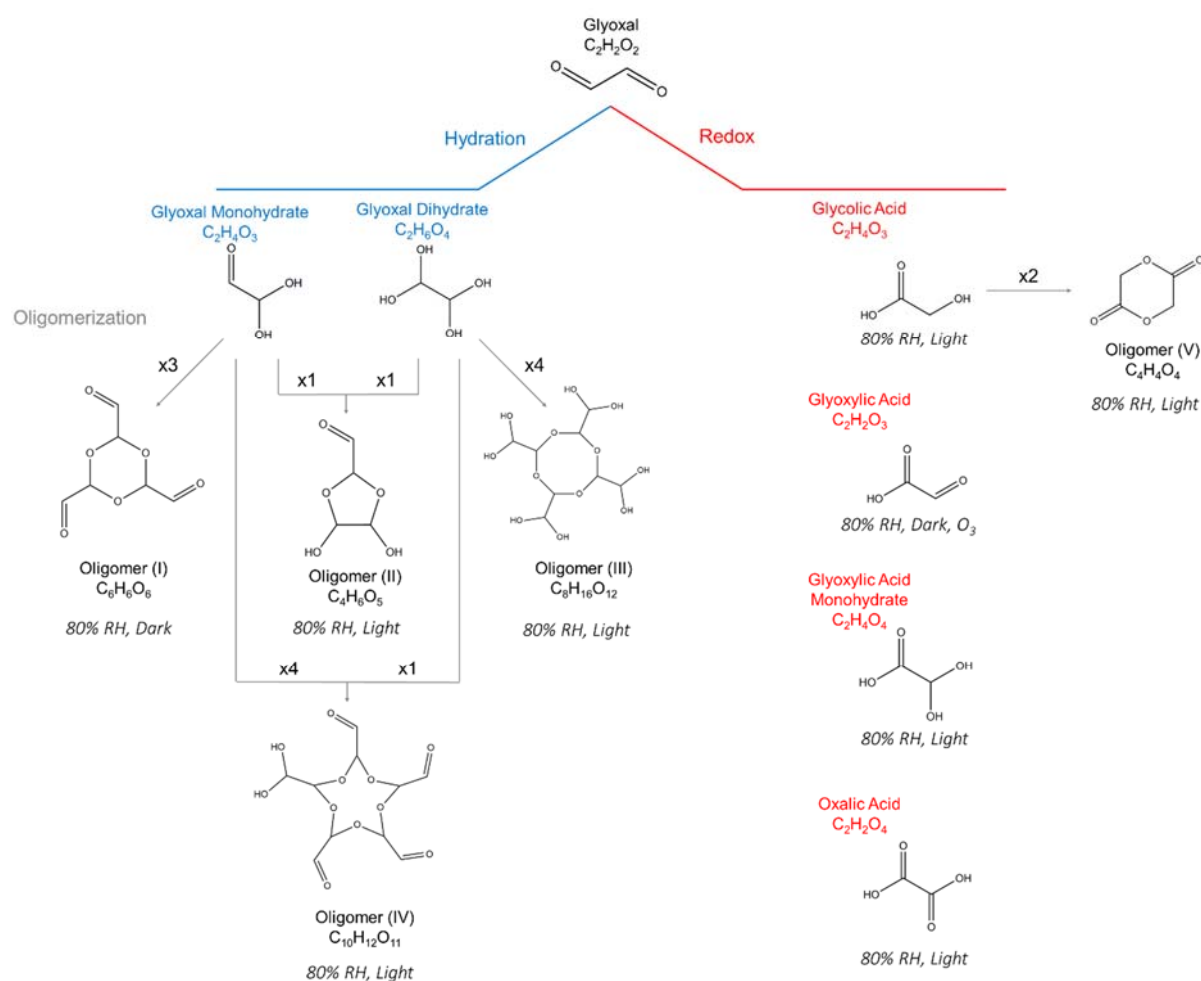
uptake), independent of glyoxal concentration. However, the steady state uptake coefficients determined after a long processing of the surface were found to decrease with increasing glyoxal concentration, due to aging of the surface.

Various reasons could induce those apparent differences. First, the differences in the experimental set up as in CESAM, the initial uptake coefficient was measured on dust aerosol particles in suspension in a large volume, compared to sieved soil (Zogka et al., 2024) and grinded mineral powders (Shen et al., 2016). The uptake coefficient is inversely proportional to the available particle surface. In our experiments, the dust available geometric surface density, calculated from the measured size distribution assuming spherical particles, is in the range $0.35\text{--}6.3 \times 10^{-3} \text{ m}^2 \text{ m}^{-3}$ (**Table 2**). As the CESAM chamber volume is equal to 4.2 m^3 , the total dust surface area available for the reaction ranges from 2 to $2.6 \times 10^{-3} \text{ m}^2$, several orders of magnitude lower than in the experiments designed by Shen et al. (2016) and Zogka et al. (2024). Shen et al. (2016) used model powders of various sizes between 35 nm and 5 μm , with BET (define BET) surface areas ranging between 1.4 and $440 \text{ m}^2 \text{ g}^{-1}$. In the conservative assumption that only 5 mg of the model powder was used, the total reactive surface area was up to 2.2 m^2 . Zogka et al. (2024) used the soil from Gobi sieved to 63 μm and a BET surface area of $10.5 \pm 1.0 \text{ m}^2 \text{ g}^{-1}$. Using even just 1 g would yield a surface area of the order of 10.5 m^2 . Differences in the results could also arise by differences in the dust mineralogy, which are difficult to ascertain in the present study.

Our estimated uptake coefficient of glyoxal on mineral dust is also nearly two orders of magnitude higher than for ammonium sulphate ($\gamma_{\text{gas-AS}} = 1.1 (\pm 0.2) \times 10^{-4}$; our study as well as Curry et al., 2018; De Haan et al., 2020; Galloway et al., 2009; Liggio et al., 2005b, a; Trainic et al., 2011), but lower than $\gamma_{\text{gas-AS}} = 2.9 \times 10^{-3}$ at a lower RH (Liggio et al., 2005). The difference could be due to the higher hygroscopicity of ammonium sulphate, enhancing water's competition with glyoxal for adsorption sites at 80% RH, when indeed ammonium sulphate is deliquescent. This suggests, nonetheless, that dust aerosols could play a very substantial role in the formation of organic aerosols at high RH compared to ammonium sulphate, which is often used as an aerosol proxy.

4.2. Mechanism of chemical transformation

Figure 7 illustrates the suggested chemical mechanisms of the transformation of gas-phase glyoxal on the mineral dust particles.



689

690 **Figure 7.** Proposed reaction scheme to explain the glyoxal-related molecular formulas detected through
 691 ESI-Orbitrap mass spectrometry and SFE/GC-MS.

692

693 The multiphase chemistry of glyoxal on mineral dust particles, leading to the formation
 694 of low-volatility, particle-phase products, is complex, involving hydration, redox, and
 695 oligomerization pathways. The chemical transformation of glyoxal upon uptake by
 696 mineral dust particles primarily occurs through aqueous-phase reactions. The
 697 mechanism is initiated by the hydration of glyoxal's aldehyde groups, forming mono-
 698 and di-hydrated species. These hydrated intermediates undergo condensation
 699 reactions, which involve nucleophilic attack and lead to the formation of cyclic acetal
 700 structures, particularly from two to five-membered dioxolane rings. This mechanism is
 701 well supported by prior studies (Loeffler et al., 2006; Kua et al., 2008; Hastings et al.,
 702 2005), which have described similar pathways for glyoxal oligomerization in aqueous
 703 environments.

This study provides new insight into this chemistry on mineral surfaces. While previous research has shown that glyoxal typically forms dimers and trimers in aqueous solution (Liggio et al., 2005; Nozière et al., 2009), our mass spectral data reveal the presence of oligomeric species containing up to 5 glyoxal units. This higher degree of oligomerization - also observed by Shen et al. (2016) - suggests that the particle-phase environment allows for extended oligomer growth. The likely contributing factors include reduced water activity, surface confinement, and enhanced proximity of reactants, all of which promote successive addition reactions that may be hindered in bulk solution (Gomez et al., 2015; Avzianova & Brooks, 2013). Concerning hydration reactions, Shen et al. (2016) showed that both glyoxal and water can accumulate onto dust particle surfaces (as evidenced by FTIR spectra), promoting hydration reactions through surface confinement of the reagents. Absorption of water on dust surfaces can also promote oligomerisation, both directly (hydration is the first step of the oligomerisation reaction) as well as indirectly by enhancing particles' ability to absorb glyoxal.

Concerning oxidation, leading to organic acid formation, the dust surface could contribute directly to this mechanism by providing redox reactive sites (Shen et al., 2016). Redox reactions promoted the formation of glycolic, glyoxylic, and oxalic acids. These compounds not only represent aging products but also participate in further condensation reactions, expanding the chemical diversity of SOA. In particular, we detected the presence of oligomer V, which we propose results not from direct glyoxal self-reactions but rather from the condensation of two glycolic acid molecules. This suggests a broader heterogeneous transformation process occurring on the dust surface, possibly involving oxidative pathways. Such cross-reactions are consistent with mechanisms proposed in glyoxal–methylglyoxal systems (Zhang et al., 2022), where mixed oligomers form through shared reaction intermediates.

A key aspect of our findings is the irreversibility of glyoxal uptake on mineral dust. In contrast to bulk aqueous systems, where glyoxal oligomerization can exist in equilibrium with monomeric species, our results suggest that oligomer formation on mineral particles is effectively irreversible. The persistence of high-molecular-weight products following drying and thermal analysis confirms that these species are chemically stable and remain in the condensed phase. This behaviour is consistent

with previous observations (Hastings et al., 2005; Ortiz-Montalvo et al., 2014) and highlights the significance of particle-phase reactions in the formation of SOA.

The acidity of the particle surface could potentially play a role in catalysing glyoxal oligomerization. It is plausible that localized acidity arises or is enhanced by the accumulation of transformation products such as glycolic and oxalic acids, which were detected in this study. This in-situ acidification may facilitate acid-catalysed reaction pathways even under neutral or weakly acidic conditions. The importance of acidity in glyoxal chemistry is supported by mechanistic proposals involving carbenium ion intermediates or hydrogen-bond-assisted nucleophilic mechanisms, which can operate effectively without requiring strongly acidic environments (Zhang et al., 2022; Gomez et al., 2015). These pathways are known to promote the formation of low-volatility oligomers, contributing to organic aerosol mass. Similarly, Ortiz-Montalvo et al. (2014) demonstrated that even mildly acidic aerosols significantly enhance glyoxal oligomerization and SOA formation.

Another critical factor is the presence of adsorbed water on mineral dust particles. Our findings demonstrate, in fact, that the availability of surface water facilitates organic aerosol formation from glyoxal. This agrees with chamber and field studies (Hastings et al., 2005; Shen et al., 2016) that identified a RH threshold above which glyoxal uptake dramatically increases. The presence of a thin aqueous film on the particle surface creates a reactive medium where glyoxal can concentrate, hydrate, and polymerize efficiently. Even after evaporation, the products formed are retained in the particle phase, evidencing their low volatility and chemical resilience.

4.3. Implications for the dust properties

The irreversible transformation of the chemical composition of mineral dust following the uptake of glyoxal could influence the physico-chemical properties of mineral dust particles. The formation of organic acids (glycolic, glyoxylic and oxalic acids) should change the dust pH, increasing its acidity and ability to dissolve transition metals like iron and copper. This could alter their speciation, enhancing their bioavailability in aqueous aerosol environments and potentially impacting atmospheric chemistry and the reactivity of aerosol particles (Giorio et al., 2022). Changes in dust pH could also affect its hygroscopic properties, influencing its ability to adsorb water and grow in size. This is consistent with our observation regarding the volume increase of dust particles after the uptake and the subsequent growth that enhances particle interaction with light

and cloud droplets formation. Collectively, these processes highlight how aerosol acidity modulates not only chemical transformations but also key physical properties and atmospheric lifetimes of dust-glyoxal systems.

The newly formed organic matter from glyoxal on dust particles could also alter the aerosol's optical properties, affecting its ability to absorb solar radiation, as recently observed in aqueous solution (De Haan et al., 2023) or on ammonium sulphate aerosols (De Haan et al. 2020; Trainic et al. 2011). The presence of hydrated glyoxal oligomeric structures has already been observed to have UV radiation absorption properties (Kalberer et al., 2004; Shapiro et al., 2009). Glyoxal-derived oligomers could significantly influence the optical properties of mineral dust aerosols. Spectroscopic analyses revealed that these oligomers have broadened OH and C–O bands and enhanced Raman activity, indicative of their hydrated and cyclic structures (Avzianova and Brooks, 2013). They also have strong UV-visible absorption, particularly between 300–600 nm, with characteristic shoulders at ~280 and 345 nm attributed to acetal and aldol condensation products (Schwier et al., 2010; Shapiro et al., 2009). High RH conditions (> 80%) facilitate brown carbon formation, evidenced by the further appearance of UV-visible absorbance peaks and Raman background signals (De Haan et al., 2020; Zhang et al., 2022).

5. Conclusions

This paper presented a novel investigation of the interaction between gas-phase glyoxal and mineral dust. By taking advantage of the capabilities of the CESAM atmospheric simulation chamber to perform multiphase experiments on time scales relevant to atmospheric processes and dispersion, including aerosols, our experiments considered airborne submicron mineral dust particles generated from a natural soil (Gobi Desert) in realistic concentrations, composition and size distribution. While airborne, the dust aerosol was aged under variable conditions of RH, irradiation, and ozone concentrations. Our study investigates, for the first time, both the rate of uptake of glyoxal and the rate of formation of the organic aerosol from the gas-phase uptake, while providing the chemical composition of the organic matter formed on the dust particles, and its implications on the particle microphysics.

This study used a single and instantaneous injection of glyoxal, and not a constant steady state flux. Above 30% RH, upon injection, glyoxal is partitioned almost

instantaneously between the gas phase, the chamber walls and the dust particles. This is an advantage to scale our results to ambient conditions. Indeed, Volkamer et al. (2005) estimated that the daytime lifetime of glyoxal is around 1.3 h. Alvarado et al. (2020) showed that the long-range transport of glyoxal produced from a point source (e.g., Canadian wildfires) may be possible only by invoking the progressive oxidation of its longer-lived precursors in the plume. In the scenario where dust aerosols interact with a glyoxal plume from a point source, one can expect an interaction time of a few minutes, compatible with that of this study. Furthermore, because the uptake follows a first-order kinetics, the measured uptake coefficient ($\gamma = (9 \pm 5) \times 10^{-3}$ at 80% RH) is independent of the glyoxal concentration and transferable to atmospheric conditions.

The uptake of glyoxal and the formation of organic matter start as soon as the glyoxal is injected into the chamber and last approximately 20 minutes. After this time, the dust surface seems saturated, likely because of the excessive glyoxal concentrations injected in the chamber. On the other hand, the uptake coefficient measured by the loss of gas-phase glyoxal molecules agrees very well with the rate of formation of the particulate organic mass on the dust, suggesting that the totality of the mass of reacting glyoxal is condensed on the dust particles. While some of the organic matter is lost again from the dust particles due to evaporation, oligomers and organic acids are detected on the dust even after the uptake has finished, indicating that the uptake of glyoxal modifies irreversibly both the composition and the physical properties of mineral dust.

This study reveals a significant quantitative transfer of gas-phase glyoxal molecules to mineral dust aerosol surfaces, occurring within a timescale of a few minutes, underscoring the important role of dust-glyoxal interactions in the atmosphere. Our results extend the current understanding of glyoxal chemistry in atmospheric systems. While oligomerization occurs through well-established aqueous-phase pathways, we suggest that mineral dust particles facilitate, in a unique way, higher-order oligomer formation, support irreversible uptake, and possibly promote alternative reaction channels such as glycolic acid condensation. These findings underscore the importance of mineral dust surfaces as active sites for multiphase SOA formation, with implications for understanding aerosol growth, composition, and climate-relevant properties. This is also in agreement with the field observations conducted by Wang et al. (2015). Neglecting the uptake pathway on dust could result in an underestimation

of glyoxal removal from the atmosphere, potentially leading to disparities between model predictions and observed gaseous concentrations of glyoxal (Kluge et al., 2023; Ling et al., 2020; Volkamer et al., 2007; Washenfelder et al., 2011). The findings of this study also have important implications for the aerosol direct and indirect radiative effect and aerosol pH. The acidification and the oxidation of the dust aerosols by glyoxal should increase their hygroscopicity, especially under high RH conditions, affecting particle growth dynamics, phase behaviour, and cloud condensation nuclei (CCN) potential (Song and Osada, 2021). Further data analysis is ongoing to address these aspects.

Data availability. The simulation chamber experiments that support the findings of this study are available through the Database of Atmospheric Simulation Chamber Studies (DASCS) of the EUROCHAMP Data Centre ([https:// data.eurochamp.org/ data- access/ chamber-experiments/](https://data.eurochamp.org/data-access/chamber-experiments/)).

Code availability. The routine used for fitting the size distribution is available at <https://doi.org/10.5281/zenodo.8135133> (Baldo and Lu, 2023). Note that in this study, we only used the size distribution measured by the OPC instrument, which was fitted with a lognormal function. The Tof-ACSM data processing (including mass calibration, peaks integration and air beam correction of ion intensities) was conducted with Tofware version 3_2_40209, the ACSM data analysis package for the software Igor Pro 7.08 (Wavemetrics, Inc., Portland, OR, USA). SFE-GC-MS data analysis was conducted using the proprietary software (TurboMass Version 6.1.0.1965 PerkinElmer®).

Author contributions. PF, JFD and FB conceptualized the study. PF and FB led the paper writing, with contributions from all the authors. JFD provided with expertise on multi-phase chemistry. CB analysed the aerosol size distribution data. VM supervised the analysis of PTR-MS data. FB, CG and DLP performed the ESI-Orbitrap analysis of filter samples. FB and JFB performed the analysis of ACSM observations. FB, TB and AG performed the SFE/CG-MS analysis of filter samples. FB, GN and SC performed the thermo-optical analysis of filter samples. FB, MC, AB, EP, VM, BPV and PF conducted the chamber experiments. MR provided with the soil sample and expertise on heterogeneous chemistry. PF provided with funding.

Competing interests. The authors declare no competing interests.

Special issue statement. This article is not part of a special issue. It is not associated with a conference.

Acknowledgements. The AERIS data center (www.aeris-data.fr) is acknowledged for distributing and curing the data produced by the CESAM chamber through the hosting of the EUROCHAMP data center (<https://data.eurochamp.org>). The initial contribution of M. Giordano (Afri-SET) to the conceptualisation of the project is gratefully acknowledged. The authors wish to thank the two anonymous referees for helping to improve the manuscript.

Financial support. This work has received funding from the French National Research Agency (ANR) through the research project CLIMDO under the grant number ANR-19-CE01-0008-02. It has received support from the European Union's Horizon 2020 research and innovation program through the EUROCHAMP-2020 Infrastructure Activity under grant agreement no. 730997. CNRS-INSU is gratefully acknowledged for supporting the CESAM chamber as a national facility as part of the French ACTRIS Research Infrastructure. ESI-

879 Orbitrap analyses was supported by a BP next generation fellowship awarded by the Yusuf
880 Hamied Department of Chemistry at the University of Cambridge to CG.

881 References

- 882 Adebisi, A., Kok, J. F., Murray, B. J., Ryder, C. L., Stuut, J.-B. W., Kahn, R. A., Knippertz, P., Formenti,
883 P., Mahowald, N. M., Pérez García-Pando, C., Klose, M., Ansmann, A., Samset, B. H., Ito, A.,
884 Balkanski, Y., Di Biagio, C., Romanias, M. N., Huang, Y., and Meng, J.: A review of coarse mineral
885 dust in the Earth system, *Aeolian Research*, 60, 100849, <https://doi.org/10.1016/j.aeolia.2022.100849>, 2023.
- 887 Aiken, A. C., DeCarlo, P. F., Kroll, J. H., Worsnop, D. R., Huffman, J. A., Docherty, K. S., Ulbrich, I. M.,
888 Mohr, C., Kimmel, J. R., Sueper, D., Sun, Y., Zhang, Q., Trimborn, A., Northway, M., Ziemann,
889 P. J., Canagaratna, M. R., Onasch, T. B., Alfarra, M. R., Prevot, A. S. H., Dommen, J., Duplissy,
890 J., Metzger, A., Baltensperger, U., and Jimenez, J. L.: O/C and OM/OC Ratios of Primary,
891 Secondary, and Ambient Organic Aerosols with High-Resolution Time-of-Flight Aerosol Mass
892 Spectrometry, *Environ. Sci. Technol.*, 42, 4478–4485, <https://doi.org/10.1021/es703009q>, 2008.
- 893 Alvarado, L. M. A., Richter, A., Vrekoussis, M., Hilboll, A., Kalisz Hedegaard, A. B., Schneising, O., and
894 Burrows, J. P.: Unexpected long-range transport of glyoxal and formaldehyde observed from the
895 Copernicus Sentinel-5 Precursor satellite during the 2018 Canadian wildfires, *Atmos. Chem.*
896 *Phys.*, 20, 2057–2072, <https://doi.org/10.5194/acp-20-2057-2020>, 2020.
- 897 Atkinson, J. D., Murray, B. J., Woodhouse, M. T., Whale, T. F., Baustian, K. J., Carslaw, K. S., Dobbie,
898 S., O’Sullivan, D., and Malkin, T. L.: The importance of feldspar for ice nucleation by mineral dust
899 in mixed-phase clouds, *Nature*, 498, 355–358, <https://doi.org/10.1038/nature12278>, 2013.
- 900 Avzianova, E. and Brooks, S. D.: Raman spectroscopy of glyoxal oligomers in aqueous solutions,
901 *Spectrochimica Acta Part A: Molecular and Biomolecular Spectroscopy*, 101, 40–48,
902 <https://doi.org/10.1016/j.saa.2012.09.050>, 2013.
- 903 Baldo, C., Formenti, P., Di Biagio, C., Lu, G., Song, C., Cazaunau, M., Pangui, E., Doussin, J.-F.,
904 Dagsson-Waldhauserova, P., Arnalds, O., Beddows, D., MacKenzie, A. R., and Shi, Z.: Complex
905 refractive index and single scattering albedo of Icelandic dust in the shortwave part of the
906 spectrum, *Atmos. Chem. Phys.*, 23, 7975–8000, <https://doi.org/10.5194/acp-23-7975-2023>,
907 2023.
- 908 Battaglia, F., Baldo, C., Cazaunau, M., Bergé, A., Pangui, E., Picquet-Varrault, B., Doussin, J.-F., and
909 Formenti, P.: Protocol for generating realistic submicron mono-dispersed mineral dust particles
910 in simulation chambers and laboratory experiments, *Aerosol Science and Technology*, 59, 357–
911 369, <https://doi.org/10.1080/02786826.2024.2442518>, 2025.
- 912 Bauer, S. E., Mishchenko, M. I., Lacis, A. A., Zhang, S., Perlwitz, J., and Metzger, S. M.: Do sulfate and
913 nitrate coatings on mineral dust have important effects on radiative properties and climate
914 modeling?, *J. Geophys. Res.*, 112, D06307, <https://doi.org/10.1029/2005JD006977>, 2007.
- 915 Brégonzio-Rozier, L., Giorio, C., Siekmann, F., Pangui, E., Morales, S. B., Temime-Roussel, B., Gratien,
916 A., Michoud, V., Cazaunau, M., DeWitt, H. L., Tapparo, A., Monod, A., and Doussin, J.-F.:
917 Secondary organic aerosol formation from isoprene photooxidation during cloud condensation–
918 evaporation cycles, *Atmos. Chem. Phys.*, 16, 1747–1760, [https://doi.org/10.5194/acp-16-1747-](https://doi.org/10.5194/acp-16-1747-2016)
919 2016, 2016.
- 920 Buxton, G. V., Malone, T. N., and Arthur Salmon, G.: Oxidation of glyoxal initiated by OH in oxygenated
921 aqueous solution, *Faraday Trans.*, 93, 2889–2891, <https://doi.org/10.1039/a701468f>, 1997.
- 922 Carlton, A. G., Turpin, B. J., Altieri, K. E., Seitzinger, S., Reff, A., Lim, H.-J., and Ervens, B.: Atmospheric
923 oxalic acid and SOA production from glyoxal: Results of aqueous photooxidation experiments,
924 *Atmospheric Environment*, 41, 7588–7602, <https://doi.org/10.1016/j.atmosenv.2007.05.035>,
925 2007.
- 926 Castellanos, P., Colarco, P., Espinosa, W. R., Guzewich, S. D., Levy, R. C., Miller, R. L., Chin, M., Kahn,
927 R. A., Kemppinen, O., Moosmüller, H., Nowottnick, E. P., Rocha-Lima, A., Smith, M. D., Yorks, J.
928 E., and Yu, H.: Mineral dust optical properties for remote sensing and global modeling: A review,
929 *Remote Sensing of Environment*, 303, 113982, <https://doi.org/10.1016/j.rse.2023.113982>, 2024.
- 930 Chan, C., Jacob, D. J., Marais, E. A., Yu, K., Travis, K. R., Kim, P. S., Fisher, J. A., Zhu, L., Wolfe, G.
931 M., Hanisco, T. F., Keutsch, F. N., Kaiser, J., Min, K.-E., Brown, S. S., Washenfelder, R. A.,

932 González Abad, G., and Chance, K.: Glyoxal yield from isoprene oxidation and relation to
 933 formaldehyde: chemical mechanism, constraints from SENEX aircraft observations, and
 934 interpretation of OMI satellite data, *Atmos. Chem. Phys.*, 17, 8725–8738,
 935 <https://doi.org/10.5194/acp-17-8725-2017>, 2017.

936 Chen, S., Chen, J., Zhang, Y., Lin, J., Bi, H., Song, H., Chen, Y., Lian, L., Liu, C., and Zhang, R.:
 937 Anthropogenic dust: sources, characteristics and emissions, *Environ. Res. Lett.*, 18, 103002,
 938 <https://doi.org/10.1088/1748-9326/acf479>, 2023.

939 Chirizzi, D.: Influence of Saharan dust outbreaks and carbon content on oxidative potential of water-
 940 soluble fractions of PM_{2.5} and PM₁₀, *Atmospheric Environment*, 2017.

941 Crowley, J. N., Ammann, M., Cox, R. A., Hynes, R. G., Jenkin, M. E., Mellouki, A., Rossi, M. J., Troe,
 942 J., and Wallington, T. J.: Evaluated kinetic and photochemical data for atmospheric chemistry:
 943 Volume V – heterogeneous reactions on solid substrates, *Atmos. Chem. Phys.*, 10, 9059–9223,
 944 <https://doi.org/10.5194/acp-10-9059-2010>, 2010.

945 De Haan, D. O., Hawkins, L. N., Jansen, K., Welsh, H. G., Pednekar, R., De Loera, A., Jimenez, N. G.,
 946 Tolbert, M. A., Cazaunau, M., Gratien, A., Bergé, A., Pangui, E., Formenti, P., and Doussin, J.-
 947 F.: Glyoxal's impact on dry ammonium salts: fast and reversible surface aerosol browning, *Atmos.*
 948 *Chem. Phys.*, 20, 9581–9590, <https://doi.org/10.5194/acp-20-9581-2020>, 2020.

949 De Haan, D. O., Hawkins, L. N., Wickremasinghe, P. D., Andretta, A. D., Dignum, J. R., De Haan, A. C.,
 950 Welsh, H. G., Pennington, E. A., Cui, T., Surratt, J. D., Cazaunau, M., Pangui, E., and Doussin,
 951 J.-F.: Brown Carbon from Photo-Oxidation of Glyoxal and SO₂ in Aqueous Aerosol, *ACS Earth*
 952 *Space Chem.*, 7, 1131–1140, <https://doi.org/10.1021/acsearthspacechem.3c00035>, 2023.

953 Denjean, C., Formenti, P., Picquet-Varrault, B., Katrib, Y., Pangui, E., Zapf, P., and Doussin, J. F.: A
 954 new experimental approach to study the hygroscopic and optical properties of aerosols:
 955 application to ammonium sulfate particles, *Atmos. Meas. Tech.*, 7, 183–197,
 956 <https://doi.org/10.5194/amt-7-183-2014>, 2014.

957 Di Biagio, C., Formenti, P., Balkanski, Y., Caponi, L., Cazaunau, M., Pangui, E., Journet, E., Nowak, S.,
 958 Caquineau, S., Andreae, M. O., Kandler, K., Saeed, T., Piketh, S., Seibert, D., Williams, E., and
 959 Doussin, J.-F.: Global scale variability of the mineral dust long-wave refractive index: a new
 960 dataset of in situ measurements for climate modeling and remote sensing, *Atmos. Chem. Phys.*,
 961 17, 1901–1929, <https://doi.org/10.5194/acp-17-1901-2017>, 2017.

962 Di Biagio, C., Formenti, P., Balkanski, Y., Caponi, L., Cazaunau, M., Pangui, E., Journet, E., Nowak, S.,
 963 Andreae, M. O., Kandler, K., Saeed, T., Piketh, S., Seibert, D., Williams, E., and Doussin, J.-F.:
 964 Complex refractive indices and single-scattering albedo of global dust aerosols in the shortwave
 965 spectrum and relationship to size and iron content, *Atmos. Chem. Phys.*, 19, 15503–15531,
 966 <https://doi.org/10.5194/acp-19-15503-2019>, 2019.

967 Dupart, Y., King, S. M., Nekat, B., Nowak, A., Wiedensohler, A., Herrmann, H., David, G., Thomas, B.,
 968 Miffre, A., Rairoux, P., D'Anna, B., and George, C.: Mineral dust photochemistry induces
 969 nucleation events in the presence of SO₂, *Proc. Natl. Acad. Sci. U.S.A.*, 109, 20842–20847,
 970 <https://doi.org/10.1073/pnas.1212297109>, 2012.

971 Ervens, B. and Volkamer, R.: Glyoxal processing by aerosol multiphase chemistry: towards a kinetic
 972 modeling framework of secondary organic aerosol formation in aqueous particles, *Atmos. Chem.*
 973 *Phys.*, 10, 8219–8244, <https://doi.org/10.5194/acp-10-8219-2010>, 2010.

974 Fröhlich, R., Cubison, M. J., Slowik, J. G., Bukowiecki, N., Prévôt, A. S. H., Baltensperger, U., Schneider,
 975 J., Kimmel, J. R., Gonin, M., Rohner, U., Worsnop, D. R., and Jayne, J. T.: The ToF-ACSM: a
 976 portable aerosol chemical speciation monitor with TOFMS detection, *Atmos. Meas. Tech.*, 6,
 977 3225–3241, <https://doi.org/10.5194/amt-6-3225-2013>, 2013.

978 Fu, T.-M., Jacob, D. J., Wittrock, F., Burrows, J. P., Vrekoussis, M., and Henze, D. K.: Global budgets
 979 of atmospheric glyoxal and methylglyoxal, and implications for formation of secondary organic
 980 aerosols, *J. Geophys. Res.*, 113, D15303, <https://doi.org/10.1029/2007JD009505>, 2008.

981 Galloway, M. M., Chhabra, P. S., Chan, A. W. H., Surratt, J. D., Flagan, R. C., Seinfeld, J. H., and
 982 Keutsch, F. N.: Glyoxal uptake on ammonium sulphate seed aerosol: reaction products and
 983 reversibility of uptake under dark and irradiated conditions, *Atmos. Chem. Phys.*, 2009.

984 Giorio, C., Monod, A., Brégonzio-Rozier, L., DeWitt, H. L., Cazaunau, M., Temime-Roussel, B., Gratien,
 985 A., Michoud, V., Pangui, E., Ravier, S., Zielinski, A. T., Tapparo, A., Vermeylen, R., Claeys, M.,
 986 Voisin, D., Kalberer, M., and Doussin, J.-F.: Cloud Processing of Secondary Organic Aerosol from
 987 Isoprene and Methacrolein Photooxidation, *J. Phys. Chem. A*, 121, 7641–7654,
 988 <https://doi.org/10.1021/acs.jpca.7b05933>, 2017.

989 Giorio, C., D'Aronco, S., Di Marco, V., Badocco, D., Battaglia, F., Soldà, L., Pastore, P., and Tapparo,
 990 A.: Emerging investigator series: aqueous-phase processing of atmospheric aerosol influences
 991 dissolution kinetics of metal ions in an urban background site in the Po Valley, *Environ. Sci.:
 992 Processes Impacts*, 24, 884–897, <https://doi.org/10.1039/D2EM00023G>, 2022.

993 Gomez, M. E., Lin, Y., Guo, S., & Zhang, R. (2015). Heterogeneous Chemistry of Glyoxal on Acidic
 994 Solutions. An Oligomerization Pathway for Secondary Organic Aerosol Formation. *The Journal of
 995 Physical Chemistry A*, 119(19), 4457–4463. <https://doi.org/10.1021/jp509916r>

996 Goodman, A. L., Underwood, G. M., and Grassian, V. H.: Heterogeneous Reaction of NO₂:
 997 Characterization of Gas-Phase and Adsorbed Products from the Reaction, 2NO₂(g) + H₂O(a)
 998 → HONO(g) + HNO₃(a) on Hydrated Silica Particles, *J. Phys. Chem. A*, 103, 7217–7223,
 999 <https://doi.org/10.1021/jp9910688>, 1999.

1000 Guo, Y., Wang, S., Zhu, J., Zhang, R., Gao, S., Saiz-Lopez, A., and Zhou, B.: Atmospheric
 1001 formaldehyde, glyoxal and their relations to ozone pollution under low- and high-NO_x regimes in
 1002 summertime Shanghai, China, *Atmospheric Research*, 258, 105635,
 1003 <https://doi.org/10.1016/j.atmosres.2021.105635>, 2021.

1004 Harrison, S. P., Kohfeld, K. E., Roelandt, C., and Claquin, T.: The role of dust in climate changes today,
 1005 at the last glacial maximum and in the future, *Earth-Science Reviews*, 54, 43–80,
 1006 [https://doi.org/10.1016/S0012-8252\(01\)00041-1](https://doi.org/10.1016/S0012-8252(01)00041-1), 2001.

1007 Hastings, W. P., Koehler, C. A., Bailey, E. L., & De Haan, D. O. (2005). Secondary Organic Aerosol
 1008 Formation by Glyoxal Hydration and Oligomer Formation: Humidity Effects and Equilibrium Shifts
 1009 during Analysis. *Environmental Science & Technology*, 39(22), 8728–8735.
 1010 <https://doi.org/10.1021/es050446l>

1011 Hettiarachchi, E. and Grassian, V. H.: Heterogeneous Reactions of Phenol on Different Components of
 1012 Mineral Dust Aerosol: Formation of Oxidized Organic and Nitro-Phenolic Compounds, *ACS EST
 1013 Air*, 1, 259–272, <https://doi.org/10.1021/acsestair.3c00042>, 2024.

1014 Horowitz, A., Meller, R., and Moortgat, G. K.: The UV–VIS absorption cross sections of the α -dicarbonyl
 1015 compounds: pyruvic acid, biacetyl and glyoxal, 2001.

1016 Hu, J., Chen, Z., Qin, X., and Dong, P.: Reversible and irreversible gas–particle partitioning of dicarbonyl
 1017 compounds observed in the real atmosphere, *Atmos. Chem. Phys.*, 22, 6971–6987,
 1018 <https://doi.org/10.5194/acp-22-6971-2022>, 2022.

1019 Joshi, N., Romanias, M. N., Riffault, V., and Thevenet, F.: Investigating water adsorption onto natural
 1020 mineral dust particles: Linking DRIFTS experiments and BET theory, *Aeolian Research*, 27, 35–
 1021 45, <https://doi.org/10.1016/j.aeolia.2017.06.001>, 2017.

1022 Lai, A. C. and Nazaroff, W. W.: MODELING INDOOR PARTICLE DEPOSITION FROM TURBULENT
 1023 FLOW ONTO SMOOTH SURFACES, *Journal of Aerosol Science*, 31, 463–476,
 1024 [https://doi.org/10.1016/S0021-8502\(99\)00536-4](https://doi.org/10.1016/S0021-8502(99)00536-4), 2000.

1025 Kalberer, M., Paulsen, D., Sax, M., Steinbacher, M., Dommen, J., Prevot, A. S. H., Fisseha, R.,
 1026 Weingartner, E., Frankevich, V., Zenobi, R., and Baltensperger, U.: Identification of Polymers as
 1027 Major Components of Atmospheric Organic Aerosols, *Science*, 303, 1659–1662,
 1028 <https://doi.org/10.1126/science.1092185>, 2004.

1029 Kluge, F., Hüneke, T., Lerot, C., Rosanka, S., Rotermund, M. K., Taraborrelli, D., Weyland, B., and
 1030 Pfeilsticker, K.: Airborne glyoxal measurements in the marine and continental atmosphere:

1031 comparison with TROPOMI observations and EMAC simulations, *Atmos. Chem. Phys.*, 23, 1369–
1032 1401, <https://doi.org/10.5194/acp-23-1369-2023>, 2023.

1033 Knippertz, P. and Stuut, J.-B. W. (Eds.): *Mineral Dust: A Key Player in the Earth System*, Springer
1034 Netherlands, Dordrecht, <https://doi.org/10.1007/978-94-017-8978-3>, 2014.

1035 Knote, C., Hodzic, A., Jimenez, J. L., Volkamer, R., Orlando, J. J., Baidar, S., Brioude, J., Fast, J.,
1036 Gentner, D. R., Goldstein, A. H., Hayes, P. L., Knighton, W. B., Oetjen, H., Setyan, A., Stark, H.,
1037 Thalman, R., Tyndall, G., Washenfelder, R., Waxman, E., and Zhang, Q.: Simulation of semi-
1038 explicit mechanisms of SOA formation from glyoxal in aerosol in a 3-D model, *Atmos. Chem.*
1039 *Phys.*, 14, 6213–6239, <https://doi.org/10.5194/acp-14-6213-2014>, 2014.

1040 Kok, J. F., Adebisi, A. A., Albani, S., Balkanski, Y., Checa-Garcia, R., Chin, M., Colarco, P. R., Hamilton,
1041 D. S., Huang, Y., Ito, A., Klose, M., Li, L., Mahowald, N. M., Miller, R. L., Obiso, V., Pérez García-
1042 Pando, C., Rocha-Lima, A., and Wan, J. S.: Contribution of the world's main dust source regions
1043 to the global cycle of desert dust, *Aerosols/Atmospheric Modelling/Troposphere/Physics* (physical
1044 properties and processes), <https://doi.org/10.5194/acp-2021-4>, 2021.

1045 Kok, J. F., Storelvmo, T., Karydis, V. A., Adebisi, A. A., Mahowald, N. M., Evan, A. T., He, C., and Leung,
1046 D. M.: Mineral dust aerosol impacts on global climate and climate change, *Nat Rev Earth Environ*,
1047 4, 71–86, <https://doi.org/10.1038/s43017-022-00379-5>, 2023.

1048 Kourtchev, I., Doussin, J.-F., Giorio, C., Mahon, B., Wilson, E. M., Maurin, N., Pangui, E., Venables, D.
1049 S., Wenger, J. C., and Kalberer, M.: Molecular composition of fresh and aged secondary organic
1050 aerosol from a mixture of biogenic volatile compounds: a high-resolution mass spectrometry
1051 study, *Atmos. Chem. Phys.*, 15, 5683–5695, <https://doi.org/10.5194/acp-15-5683-2015>, 2015.

1052 Kroll, J. H., Ng, N. L., Murphy, S. M., Varutbangkul, V., Flagan, R. C., and Seinfeld, J. H.: Chamber
1053 studies of secondary organic aerosol growth by reactive uptake of simple carbonyl compounds,
1054 *J. Geophys. Res.*, 110, 2005JD006004, <https://doi.org/10.1029/2005JD006004>, 2005.

1055 Kua, J., Hanley, S. W., & De Haan, D. O. (2008). Thermodynamics and Kinetics of Glyoxal Dimer
1056 Formation: A Computational Study. *The Journal of Physical Chemistry A*, 112(1), 66–72.
1057 <https://doi.org/10.1021/jp076573g>

1058 Lewis, A. C., Hopkins, J. R., Carslaw, D. C., Hamilton, J. F., Nelson, B. S., Stewart, G., Dornie, J.,
1059 Passant, N., and Murrells, T.: An increasing role for solvent emissions and implications for future
1060 measurements of volatile organic compounds, *Phil. Trans. R. Soc. A.*, 378, 20190328,
1061 <https://doi.org/10.1098/rsta.2019.0328>, 2020.

1062 Li, G., Cheng, Y., Kuhn, U., Xu, R., Yang, Y., Meusel, H., Wang, Z., Ma, N., Wu, Y., Li, M., Williams, J.,
1063 Hoffmann, T., Ammann, M., Pöschl, U., Shao, M., and Su, H.: Physicochemical uptake and
1064 release of volatile organic compounds by soil in coated-wall flow tube experiments with ambient
1065 air, *Atmos. Chem. Phys.*, 19, 2209–2232, <https://doi.org/10.5194/acp-19-2209-2019>, 2019.

1066 Li, L., Mahowald, N. M., Miller, R. L., Pérez García-Pando, C., Klose, M., Hamilton, D. S., Gonçalves
1067 Ageitos, M., Ginoux, P., Balkanski, Y., Green, R. O., Kalashnikova, O., Kok, J. F., Obiso, V.,
1068 Paynter, D., and Thompson, D. R.: Quantifying the range of the dust direct radiative effect due to
1069 source mineralogy uncertainty, *Atmos. Chem. Phys.*, 21, 3973–4005, <https://doi.org/10.5194/acp-21-3973-2021>, 2021.

1071 Li, Q., Gong, D., Wang, H., Wang, Y., Han, S., Wu, G., Deng, S., Yu, P., Wang, W., and Wang, B.: Rapid
1072 increase in atmospheric glyoxal and methylglyoxal concentrations in Lhasa, Tibetan Plateau:
1073 Potential sources and implications, *Science of The Total Environment*, 824, 153782,
1074 <https://doi.org/10.1016/j.scitotenv.2022.153782>, 2022.

1075 Liggio, J.: Reactive uptake of glyoxal by particulate matter, *J. Geophys. Res.*, 110, D10304,
1076 <https://doi.org/10.1029/2004JD005113>, 2005a.

1077 Liggio, J., Li, S.-M., and McLaren, R.: Heterogeneous Reactions of Glyoxal on Particulate Matter:
1078 Identification of Acetals and Sulfate Esters, *Environ. Sci. Technol.*, 39, 1532–1541,
1079 <https://doi.org/10.1021/es048375y>, 2005b.

1080 Lim, Y. B., Tan, Y., Perri, M. J., Seitzinger, S. P., and Turpin, B. J.: Aqueous chemistry and its role in
 1081 secondary organic aerosol (SOA) formation, *Atmos. Chem. Phys.*, 10, 10521–10539,
 1082 <https://doi.org/10.5194/acp-10-10521-2010>, 2010.

1083 Ling, Z., Xie, Q., Shao, M., Wang, Z., Wang, T., Guo, H., and Wang, X.: Formation and sink of glyoxal
 1084 and methylglyoxal in a polluted subtropical environment: observation-based photochemical
 1085 analysis and impact evaluation, *Atmos. Chem. Phys.*, 20, 11451–11467,
 1086 <https://doi.org/10.5194/acp-20-11451-2020>, 2020.

1087 Liu, C., Chu, B., Liu, Y., Ma, Q., Ma, J., He, H., Li, J., and Hao, J.: Effect of mineral dust on secondary
 1088 organic aerosol yield and aerosol size in α -pinene/NO_x photo-oxidation, *Atmospheric*
 1089 *Environment*, 77, 781–789, <https://doi.org/10.1016/j.atmosenv.2013.05.064>, 2013.

1090 Loeffler, K. W., Koehler, C. A., Paul, N. M., & De Haan, D. O. (2006). Oligomer Formation in Evaporating
 1091 Aqueous Glyoxal and Methyl Glyoxal Solutions. *Environmental Science & Technology*, 40(20),
 1092 6318–6323. <https://doi.org/10.1021/es060810w>

1093 Mahowald, N., Albani, S., Kok, J. F., Engelstaeder, S., Scanza, R., Ward, D. S., and Flanner, M. G.: The
 1094 size distribution of desert dust aerosols and its impact on the Earth system, *Aeolian Research*,
 1095 15, 53–71, <https://doi.org/10.1016/j.aeolia.2013.09.002>, 2014.

1096 Ng, N. L., Canagaratna, M. R., Jimenez, J. L., Chhabra, P. S., Seinfeld, J. H., and Worsnop, D. R.:
 1097 Changes in organic aerosol composition with aging inferred from aerosol mass spectra, *Atmos.*
 1098 *Chem. Phys.*, 11, 6465–6474, <https://doi.org/10.5194/acp-11-6465-2011>, 2011.

1099 Nie, W., Ding, A., Wang, T., Kerminen, V.-M., George, C., Xue, L., Wang, W., Zhang, Q., Petäjä, T., Qi,
 1100 X., Gao, X., Wang, X., Yang, X., Fu, C., and Kulmala, M.: Polluted dust promotes new particle
 1101 formation and growth, *Sci Rep*, 4, 6634, <https://doi.org/10.1038/srep06634>, 2014.

1102 Nieder, R., Benbi, D. K., and Reichl, F. X.: Soil-Borne Particles and Their Impact on Environment and
 1103 Human Health, in: *Soil Components and Human Health*, Springer Netherlands, Dordrecht, 99–
 1104 177, https://doi.org/10.1007/978-94-024-1222-2_3, 2018.

1105 Nozière, B., Dziedzic, P., and Córdoba, A.: Products and Kinetics of the Liquid-Phase Reaction of
 1106 Glyoxal Catalyzed by Ammonium Ions (NH₄⁺), *J. Phys. Chem. A*, 113, 231–237,
 1107 <https://doi.org/10.1021/jp8078293>, 2009.

1108 Ooki, A. and Uematsu, M.: Chemical interactions between mineral dust particles and acid gases during
 1109 Asian dust events, *J. Geophys. Res.*, 110, 2004JD004737,
 1110 <https://doi.org/10.1029/2004JD004737>, 2005.

1111 Ortiz-Montalvo, D. L., Häkkinen, S. A. K., Schwier, A. N., Lim, Y. B., McNeill, V. F., and Turpin, B. J.:
 1112 Ammonium Addition (and Aerosol pH) Has a Dramatic Impact on the Volatility and Yield of Glyoxal
 1113 Secondary Organic Aerosol, *Environ. Sci. Technol.*, 48, 255–262,
 1114 <https://doi.org/10.1021/es4035667>, 2014.

1115 Ponczek, M., Hayeck, N., Emmelin, C., and George, C.: Heterogeneous photochemistry of dicarboxylic
 1116 acids on mineral dust, *Atmospheric Environment*, 212, 262–271,
 1117 <https://doi.org/10.1016/j.atmosenv.2019.05.032>, 2019.

1118 Romanias, M. N., El Zein, A., and Bedjanian, Y.: Heterogeneous Interaction of H₂O₂ with TiO₂
 1119 Surface under Dark and UV Light Irradiation Conditions, *J. Phys. Chem. A*, 116, 8191–8200,
 1120 <https://doi.org/10.1021/jp305366v>, 2012.

1121 Romanías, Manolis N., Habib Ourrad, Frédéric Thévenet, and Véronique Riffault. 2016. “Investigating
 1122 the Heterogeneous Interaction of VOCs with Natural Atmospheric Particles: Adsorption of
 1123 Limonene and Toluene on Saharan Mineral Dusts.” *The Journal of Physical Chemistry A*
 1124 120(8):1197–1212. doi: 10.1021/acs.jpca.5b10323.

1125 Rossignol, S., Aregahegn, K. Z., Tinel, L., Fine, L., Nozière, B., and George, C.: Glyoxal Induced
 1126 Atmospheric Photosensitized Chemistry Leading to Organic Aerosol Growth, *Environ. Sci.*
 1127 *Technol.*, 48, 3218–3227, <https://doi.org/10.1021/es405581g>, 2014.

1128 Rubasinghege, G., Ogden, S., Baltrusaitis, J., and Grassian, V. H.: Heterogeneous Uptake and
 1129 Adsorption of Gas-Phase Formic Acid on Oxide and Clay Particle Surfaces: The Roles of Surface

Hydroxyl Groups and Adsorbed Water in Formic Acid Adsorption and the Impact of Formic Acid Adsorption on Water Uptake, *J. Phys. Chem. A*, 117, 11316–11327, <https://doi.org/10.1021/jp408169w>, 2013.

Safi Shalamzari, M., Ryabtsova, O., Kahnt, A., Vermeylen, R., Hérent, M., Quetin-Leclercq, J., Van Der Veken, P., Maenhaut, W., and Claeys, M.: Mass spectrometric characterization of organosulfates related to secondary organic aerosol from isoprene, *Rapid Comm Mass Spectrometry*, 27, 784–794, <https://doi.org/10.1002/rcm.6511>, 2013.

Schwier, A. N., Sareen, N., Mitroo, D., Shapiro, E. L., and McNeill, V. F.: Glyoxal-Methylglyoxal Cross-Reactions in Secondary Organic Aerosol Formation, *Environ. Sci. Technol.*, 44, 6174–6182, <https://doi.org/10.1021/es101225q>, 2010.

Seisel, S., Lian, Y., Keil, T., Trukhin, M. E., and Zellner, R.: Kinetics of the interaction of water vapour with mineral dust and soot surfaces at T = 298 K, *Phys. Chem. Chem. Phys.*, 6, 1926–1932, <https://doi.org/10.1039/B314568A>, 2004.

Shapiro, E. L., Szprengiel, J., Sareen, N., Jen, C. N., Giordano, M. R., and McNeill, V. F.: Light-absorbing secondary organic material formed by glyoxal in aqueous aerosol mimics, *Atmos. Chem. Phys.*, 2009.

Shen, X., Wu, H., Zhao, Y., Huang, D., Huang, L., and Chen, Z.: Heterogeneous reactions of glyoxal on mineral particles: A new avenue for oligomers and organosulfate formation, *Atmospheric Environment*, 131, 133–140, <https://doi.org/10.1016/j.atmosenv.2016.01.048>, 2016.

Shrivastava, M., Cappa, C. D., Fan, J., Goldstein, A. H., Guenther, A. B., Jimenez, J. L., Kuang, C., Laskin, A., Martin, S. T., Ng, N. L., Petaja, T., Pierce, J. R., Rasch, P. J., Roldin, P., Seinfeld, J. H., Shilling, J., Smith, J. N., Thornton, J. A., Volkamer, R., Wang, J., Worsnop, D. R., Zaveri, R. A., Zelenyuk, A., and Zhang, Q.: Recent advances in understanding secondary organic aerosol: Implications for global climate forcing, *Reviews of Geophysics*, 55, 509–559, <https://doi.org/10.1002/2016RG000540>, 2017.

Song, Q. and Osada, K.: Direct measurement of aerosol acidity using pH testing paper and hygroscopic equilibrium under high relative humidity, *Atmospheric Environment*, 261, 118605, <https://doi.org/10.1016/j.atmosenv.2021.118605>, 2021.

Steinke, I., Funk, R., Busse, J., Iturri, A., Kirchen, S., Leue, M., Möhler, O., Schwartz, T., Schnaiter, M., Sierau, B., Toprak, E., Ullrich, R., Ulrich, A., Hoose, C., and Leisner, T.: Ice nucleation activity of agricultural soil dust aerosols from Mongolia, Argentina, and Germany, *JGR Atmospheres*, 121, <https://doi.org/10.1002/2016JD025160>, 2016.

Sun, Y. L., Zhang, Q., Anastasio, C., and Sun, J.: Insights into secondary organic aerosol formed via aqueous-phase reactions of phenolic compounds based on high resolution mass spectrometry, *Atmos. Chem. Phys.*, 10, 4809–4822, <https://doi.org/10.5194/acp-10-4809-2010>, 2010.

Tang, M., Huang, X., Lu, K., Ge, M., Li, Y., Cheng, P., Zhu, T., Ding, A., Zhang, Y., Gligorovski, S., Song, W., Ding, X., Bi, X., and Wang, X.: Heterogeneous reactions of mineral dust aerosol: implications for tropospheric oxidation capacity, *Atmos. Chem. Phys.*, 17, 11727–11777, <https://doi.org/10.5194/acp-17-11727-2017>, 2017.

Tegen, I. and Fung, I.: Contribution to the atmospheric mineral aerosol load from land surface modification, *J. Geophys. Res.*, 100, 18707, <https://doi.org/10.1029/95JD02051>, 1995.

Trainic, M., Abo Riziq, A., Lavi, A., Flores, J. M., and Rudich, Y.: The optical, physical and chemical properties of the products of glyoxal uptake on ammonium sulfate seed aerosols, *Atmos. Chem. Phys.*, 11, 9697–9707, <https://doi.org/10.5194/acp-11-9697-2011>, 2011.

Turpin, B. J. and Huntzicker, J. J.: Identification of secondary organic aerosol episodes and quantitation of primary and secondary organic aerosol concentrations during SCAQS, *Atmospheric Environment*, 29, 3527–3544, [https://doi.org/10.1016/1352-2310\(94\)00276-Q](https://doi.org/10.1016/1352-2310(94)00276-Q), 1995.

Usher, C. R., Michel, A. E., and Grassian, V. H.: Reactions on Mineral Dust, *Chem. Rev.*, 103, 4883–4940, <https://doi.org/10.1021/cr020657y>, 2003.

1179 Volkamer, R., Platt, U., and Wirtz, K.: Primary and Secondary Glyoxal Formation from Aromatics:
 1180 Experimental Evidence for the Bicycloalkyl-Radical Pathway from Benzene, Toluene, and p -
 1181 Xylene, *J. Phys. Chem. A*, 105, 7865–7874, <https://doi.org/10.1021/jp010152w>, 2001.

1182 Volkamer, R., Spietz, P., Burrows, J., and Platt, U.: High-resolution absorption cross-section of glyoxal
 1183 in the UV–vis and IR spectral ranges, *Journal of Photochemistry and Photobiology A: Chemistry*,
 1184 172, 35–46, <https://doi.org/10.1016/j.jphotochem.2004.11.011>, 2005.

1185 Volkamer, R., San Martini, F., Molina, L. T., Salcedo, D., Jimenez, J. L., and Molina, M. J.: A missing
 1186 sink for gas-phase glyoxal in Mexico City: Formation of secondary organic aerosol, *Geophysical*
 1187 *Research Letters*, 34, 2007GL030752, <https://doi.org/10.1029/2007GL030752>, 2007.

1188 Vrekoussis, M., Wittrock, F., Richter, A., Burrows, J. P., and Cho, C.: Temporal and spatial variability of
 1189 glyoxal as observed from space, *Atmos. Chem. Phys.*, 2009.

1190 Wagner, C., Hanisch, F., Holmes, N., de Coninck, H., Schuster, G., and Crowley, J. N.: The interaction
 1191 of N₂O₅ with mineral dust: aerosol flow tube and Knudsen reactor studies, *Atmos. Chem. Phys.*,
 1192 2008.

1193 Walker, H., Stone, D., Ingham, T., Hackenberg, S., Cryer, D., Punjabi, S., Read, K., Lee, J., Whalley,
 1194 L., Spracklen, D. V., Carpenter, L. J., Arnold, S. R., and Heard, D. E.: Observations and modelling
 1195 of glyoxal in the tropical Atlantic marine boundary layer, *Atmos. Chem. Phys.*, 22, 5535–5557,
 1196 <https://doi.org/10.5194/acp-22-5535-2022>, 2022.

1197 Wang, G., Cheng, C., Meng, J., Huang, Y., Li, J., and Ren, Y.: Field observation on secondary organic
 1198 aerosols during Asian dust storm periods: Formation mechanism of oxalic acid and related
 1199 compounds on dust surface, *Atmospheric Environment*, 113, 169–176,
 1200 <https://doi.org/10.1016/j.atmosenv.2015.05.013>, 2015.

1201 Wang, J., Doussin, J. F., Perrier, S., Perraudin, E., Katrib, Y., Pangu, E., and Picquet-Varrault, B.:
 1202 Design of a new multi-phase experimental simulation chamber for atmospheric photochemistry,
 1203 aerosol and cloud chemistry research, *Atmos. Meas. Tech.*, 4, 2465–2494,
 1204 <https://doi.org/10.5194/amt-4-2465-2011>, 2011.

1205 Washenfelder, R. A., Young, C. J., Brown, S. S., Angevine, W. M., Atlas, E. L., Blake, D. R., Bon, D. M.,
 1206 Cubison, M. J., De Gouw, J. A., Dusanter, S., Flynn, J., Gilman, J. B., Graus, M., Griffith, S.,
 1207 Grossberg, N., Hayes, P. L., Jimenez, J. L., Kuster, W. C., Lefer, B. L., Pollack, I. B., Ryerson, T.
 1208 B., Stark, H., Stevens, P. S., and Trainer, M. K.: The glyoxal budget and its contribution to organic
 1209 aerosol for Los Angeles, California, during CalNex 2010: GLYOXAL BUDGET FOR LOS
 1210 ANGELES, *J. Geophys. Res.*, 116, <https://doi.org/10.1029/2011JD016314>, 2011.

1211 Webb, N. P. and Pierre, C.: Quantifying Anthropogenic Dust Emissions, *Earth's Future*, 6, 286–295,
 1212 <https://doi.org/10.1002/2017EF000766>, 2018.

1213 Xu, K., Liu, Y., Li, C., Zhang, C., Liu, X., Li, Q., Xiong, M., Zhang, Y., Yin, S., and Ding, Y.: Enhanced
 1214 secondary organic aerosol formation during dust episodes by photochemical reactions in the
 1215 winter in Wuhan, *Journal of Environmental Sciences*, 133, 70–82,
 1216 <https://doi.org/10.1016/j.jes.2022.04.018>, 2023.

1217 Zeineddine, M. N., Romanias, M. N., Gaudion, V., Riffault, V., and Thévenet, F.: Heterogeneous
 1218 Interaction of Isoprene with Natural Gobi Dust, *ACS Earth Space Chem.*, 1, 236–243,
 1219 <https://doi.org/10.1021/acsearthspacechem.7b00050>, 2017.

1220 Zeineddine, M. N., Urupina, D., Romanias, M. N., Riffault, V., and Thevenet, F.: Uptake and reactivity
 1221 of acetic acid on Gobi dust and mineral surrogates: A source of oxygenated volatile organic
 1222 compounds in the atmosphere?, *Atmospheric Environment*, 294, 119509,
 1223 <https://doi.org/10.1016/j.atmosenv.2022.119509>, 2023.

1224 Zhang, X., He, A., Guo, R., Zhao, Y., Yang, L., Morita, S., Xu, Y., Noda, I., and Ozaki, Y.: A new approach
 1225 to removing interference of moisture from FTIR spectrum, *Spectrochimica Acta Part A: Molecular*
 1226 *and Biomolecular Spectroscopy*, 265, 120373, <https://doi.org/10.1016/j.saa.2021.120373>, 2022.

1227 Zhang, Y., He, L., Sun, X., Ventura, O. N., & Herrmann, H. (2022). Theoretical Investigation on the
 1228 Oligomerization of Methylglyoxal and Glyoxal in Aqueous Atmospheric Aerosol Particles. *ACS*

1229 Earth and Space Chemistry, 6(4), 1031–1043.
1230 <https://doi.org/10.1021/acsearthspacechem.1c00422>

1231 Zielinski, A. T., Kourtchev, I., Bortolini, C., Fuller, S. J., Giorio, C., Popoola, O. A. M., Bogialli, S.,
1232 Tapparo, A., Jones, R. L., and Kalberer, M.: A new processing scheme for ultra-high resolution
1233 direct infusion mass spectrometry data, *Atmospheric Environment*, 178, 129–139,
1234 <https://doi.org/10.1016/j.atmosenv.2018.01.034>, 2018.

1235

1236